NANOMECHANICAL CHARACTERIZATION OF TOBACCO MOSAIC VIRUS SUPERLATTICE WITH NOVEL ATOMIC FORCE MICROSCOPY METHODS

A Thesis
Submitted to the Graduate Faculty
of the
North Dakota State University
of Agriculture and Applied Science

By

Haoran Wang

In Partial Fulfillment of the Requirements
For the Degree of
MASTER OF SCIENCE

Major Department:
Mechanical Engineering

May 2013

Fargo, North Dakota

North Dakota State University
Graduate School

Title

NANOMECHANICAL CHARACTERIZATION OF
TOBACCO MOSAIC VIRUS SUPERLATTICE
WITH NOVEL ATOMIC FORCE MICROSCOPY METHODS

By

Haoran Wang

The Supervisory Committee certifies that this ***disquisition*** complies with North Dakota State University's regulations and meets the accepted standards for the degree of

MASTER OF SCIENCE

SUPERVISORY COMMITTEE:

Dr. Xinnan Wang
Chair

Dr. Annie Tangpong

Dr. Chad Ulven

Dr. Jing Shi

Approved:

May 21, 2013	Alan Kallmayer
Date	Department Chair

ABSTRACT

Tobacco mosaic virus (TMV) has been widely studied due to its excellent properties. In order to utilize TMV superlattice, this thesis initiates the study on its mechanical properties.

The elastic modulus of TMV superlattice was first assessed by means of AFM-based nanoindentation and extended JKR model. The consideration of adhesion involved in the interaction of the AFM tip and the surface of the sample results in more accurate measurement. The novel numerical process proposed in this thesis simplifies the fitting procedure.

The viscoelasticity of TMV superlattice was also measured. The AFM was for the first time utilized to perform a transient viscoelastic experiment. An adhesive viscoelastic contact mechanics model was developed based on which the elastic moduli E, E_2 and the viscosity η (Fig.4.5) are determined to be 3 GPa, 0.0213 GPa and 12.4 GPa.ms, respectively.

This thesis can serve as novel examples to characterize the mechanical properties of nano-biomaterials.

ACKNOWLEDGEMENTS

I would like to pay more great appreciation to my academic advisor, Dr. Xinnan Wang. He supported my master's study in the department of mechanical engineering. I really enjoy the discussion with him, where some good ideas can be inspired. Dr. Wang paid a lot of time and energy on my research papers and thesis writing. Besides, his wealthy knowledge in experimental nanomechanics does help me a lot.

My thanks should be given to Dr. Tao Li at Argonne National Lab in Chicago, too. Without his generosity in shearinghis findings and knowledge as well as some experiments performed by him, I cannot come into contact with such an exciting research topic.

I also wish to express my gratitude to Dr. Tangpong, Dr. Ulven and Dr. Shi for serving as my committee members and providing some valuable suggestion on my thesis writing. Thank you for your time spent on reading my thesis and joining in my defense.

TABLE OF CONTENTS

LIST OF TABLES

LIST OF FIGURES

LIST OF APPENDIX FIGURES

CHAPTER 1. INTRODUCTION

Since the discovery of the first virus at the end of 19th century [1], numerical research has been sparked to make good biomedical use of virus. As a premise for practical uses,the availability and reliability of virus should be guaranteed.It has been found that many viruses feature simplicity of virus isolation and continuous storage stabilities.[2] The self-assembly of viruses could assist in drugs or imaging agents packing.[3],[4] The outer shell of the virus, which is a densely organized coat protein, can be furnished with peptides by means of chemical or genetic modification for nucleation and growth of nanomaterials.[4-7] Viruses were also employed as the carrier for recombinant protein expressions or for gene silencing studies.[8-10]

Tobacco mosaic virus (TMV) has been intensively studied as a subject of model system for biochemistry and nanomaterial during the past five decades.[11]It has a single strand RNA coated and protected by more than 2130 protein molecules (displayed in Fig.1.1). The helically arranged coat protein is shown in Fig.1.2. An individual TMV has a special tubular structure with a length of 300 nm, an inner diameter of 4 nm and an outer diameter of 18 nm.[12] However, the TMVs observed under microscope are usually longer than 300 nm due to the head-to-tail self-assembly.[13] Intriguing properties have been found in TMVs, such as the ease of culture and thermo-stability. More than 100 plants can serve as its host and the TMVs can transfer by simple contact between those hosts and its vectors.[14] It has been found that, TMVs on a host leaf can keep alive for 30 minutes even under the temperature of 50 degrees Celsius. Besides of that, the lowest free energy resulted by the way the RNA and proteins are assembled by themselves leads to the most stable structure. TMV is the first virus observed to be able to crystallize, and, interestingly, crystallized TMVs keep active. The index of refraction of TMVs is

1.57 and its isoelectric point is 3.4.[15] The surface of TMVs is charged negatively in a neutral-PH surrounding.

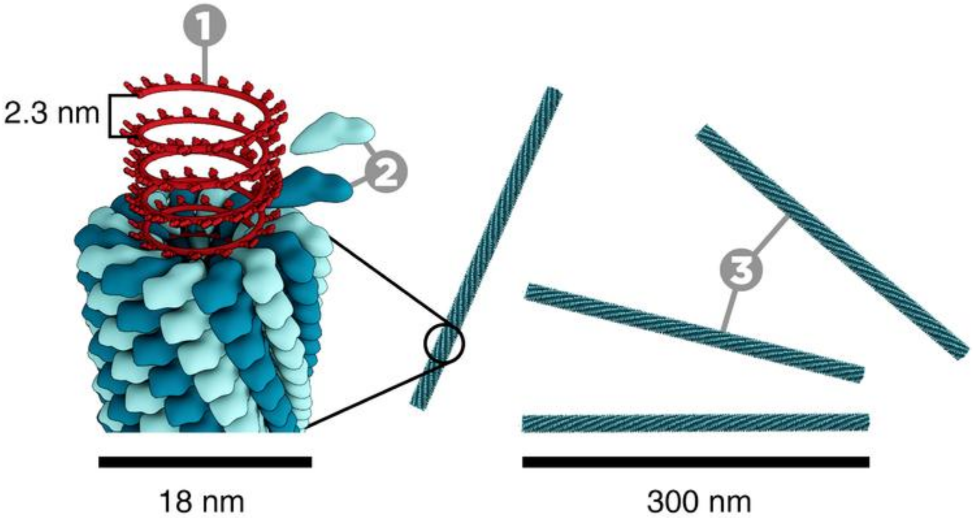

Figure 1.1. TMV structures.[16]

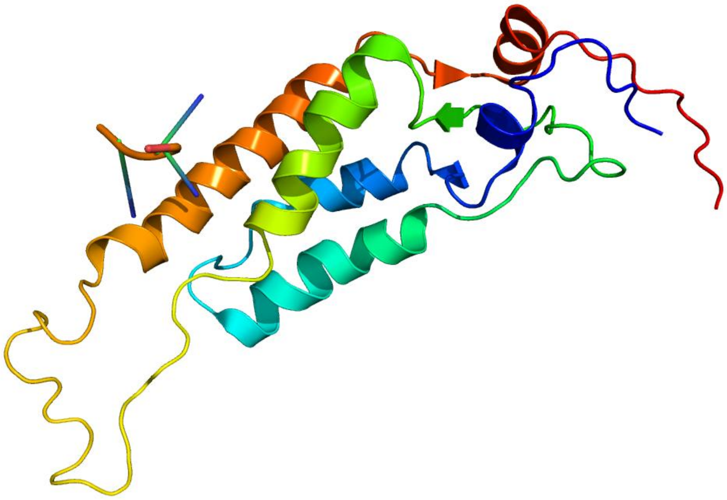

Figure 1.2. The helical arrangement of the TMV coat protein.[17]

Besides of the properties mentioned above, scientists have been also trying to bring some practical value to TMVs. It has shown that TMV mutant can successfully guide the cell adhesion differentiation and morphologies by using TMV mutants as extracellular matrix proteins.[2] Besides, it was confirmed that cell spreading, migration and differentiation can be adjusted by

TMV's functionalities and its assembly patterns achieved by chemically or genetically changing its surface properties.[18] TMV was also electrospun with polyvinyl alcohol (PVA) into continuous TMV–PVA composite nanofibers. Those nanofibers are able to form biodegradable nonwoven fibrous mat which can be used as an extracellular matrix mimetic.[19] A recent study fabricated a bio-inorganic nanostructure by soaking TMVs into platinum nanoparticles and forming cluster between the inorganic particles and the coat protein of TMVs. The newly fabricated nanostructure is able to achieve the function of on/off switch and thus can be used in nanoelectronic devices.[20]

Recently, a 2-D hexagonally-packed rod-like superlattice structure has been synthesized by mixing TMV solution with Ba^{2+},[21] as shown schematically in Fig.1.3.Zn^{2+}, Ca^{2+}, Mg^{2+}, and Cd^{2+} were found to be unable to trigger the formation of the superlattice. Only when the molar ratio of Ba^{2+}/TMV is above 9.2×10^4, crystallized lattice can be formed by the assembly of TMV and precipitate out. Otherwise, TMVs exist in a colloid state which is separated from the transparent solution. This is observed by energy dispersion X-ray (EDX). EDX and X-ray transmittance measurement revealed that Ba ions are mainly distributed in the white precipitation phase and the newly formed superlattice bundle also contains Ba ions, as shown in Fig.1.4(b) where the crossing in (a) is chosen for EDX analysis and the results are presented in (b). This indicates that Ba ions play a driving role in the assembly of TMV. GNOM fits and the pair distance distribution function (PDDF) shows that the pair distance of TMVs in precipitation is larger than its cross-section diameter, 18nm. This is another proof that Ba ions are distributed on the surfaces of TMVs. All these facts lead to the conclusion that Ba ions give rise to like-charge forces on the surfaces of TMVs which accordingly get TMV fibers together. The distance between the centers of two neighboring TMVs are ~21.6nm and it remains the same regardless of the PH value and molar ratio of Ba^{2+}/TMV (as long as it's above the critical ratio).

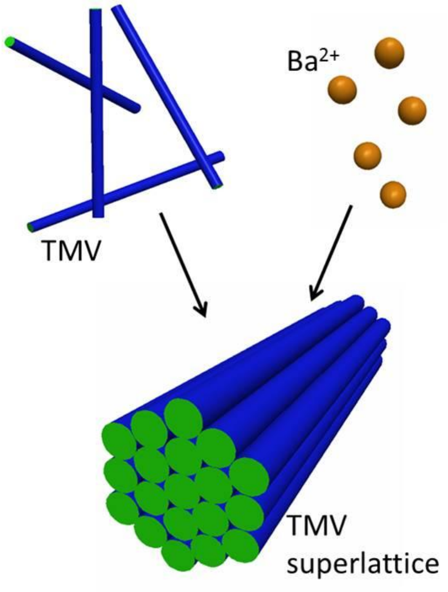

Figure 1.3. 2-D hexagonal packing of TMVs to form superlattice.

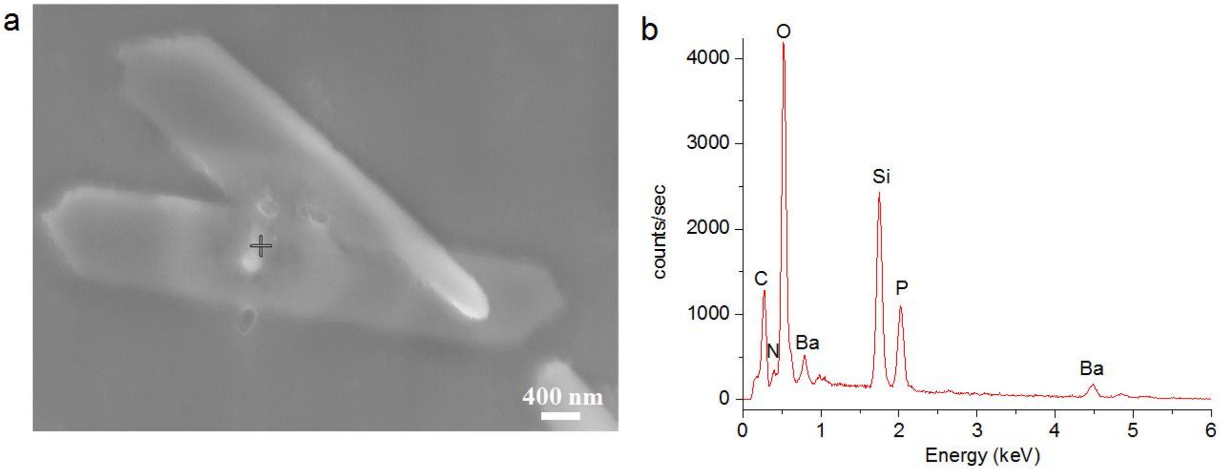

Figure 1.4. EDX analysis results of TMV superlattice.

Superlattice is a periodic structure of two or more layers of different materials stacking on top of one another. Its properties can be drastically different from its constituents. Since its discovery in the early 1920s, due to their enhanced and alterable properties, a number of superlattice structures formed by inorganic materials have been constructed and used in a host of technological applications.[22-25]The synthesized TiN/NbN superlattice films and annealed Si/SiGe strained-layer superlattice are excellent wear-resistant materials because of their significantly high shear resistance.[26, 27] Carbon nanotube (CNT) superlattice presents an electronic-band structure and optical absorption that differ dramatically from its CNT counterparts.[28, 29]Gold nanorod superlattice has been utilized for electronic storage and plasmonic waveguide.[30-32] Those fantastic properties achieved by superlattice and the discovery of the TMV superlattice formation guide us to the idea that TMV superlattice possibly have some very unique and potentially valuable features. As a result, the biomedical and industrial uses of TMVs may be extended to a wider range.

These promising biomedical applications of TMV and TMV-based nanomaterials, however, need both the biochemical and mechanical studies. For example, the elastic moduli of the small organisms in human circulatory system, such as the red blood cells and the vaccine or drug carriers, are related to the viscosity of blood. If TMV superlattice is employed for drug delivery uses, the effect on the viscosity of blood by the addition of TMV superlattice should be an important aspect for consideration. In addition, the flow rate in the capillaries is dependent on the deformability of those particles transported in blood, which in turn directly influences the safety of the patient.[33] The surface energy density of micro/nano-particles highly influences the bio-adhesive properties. There are definitely a lot of other reasons for which it is really necessary for us to study the mechanical properties of TMV and TMV superlattice formed in Ba ions solution. Mechanical properties of TMV and TMV-based nanomateirals have been characterized during the last two decades via different testing methodologies. Falvo *et al.* studied a single TMV using atomic force microscopy (AFM) combined with a real-time microscope control interface. The flexural rigidity of $5.5\times10^{-24}\ \mathrm{N\cdot m^2}$ and the elastic modulus 1.1 GPa were reported.[34] Schmatulla *et al.* predicted that the elastic moduli of TMV were of 6.8 GPa and 5.0 GPa using static method and dynamic method, respectively.[35] The polyaniline coated TMV nanotubes were characterized with AFM nanoindentation technique and an elastic modulus of 1.26 GPa was estimated based on the finite element modeling (FEM).[13] Most recently, Zhao *et al.* obtained the radial elasticity of TMV by both FEM simulation and Hertz theoretical analysis, which was consistent with what Falvo *et al.* reported.[36] Besides to the elastic modulus, viscoelasticity is also a significant parameter of biomaterials, which is however, more challenging to be measured in micro and even nanometer scale. Quite a few techniques to measure the viscoelasticity of macro-scale materials have been developed and widely used. A comprehensive review of those methods can be found in reference [37], which covers the principles of viscoelasticity, experimental setup for time-domain and frequency-domain measurements. When a sample under investigation is scaled down to micro or even nanometer, the viscoelastic measurements are complicated by the complexity of interaction between the probe and the sample. However, the knowledge of the micro/nano biomaterials, such the virus, cell and cytoskeleton, is of great importance for a better understanding of some key physiological phenomena. Before this, efforts have been made to assess the viscoelasticity of micro/nano materials with a contact-resonance atomic force microscope (AFM) [38-40]. The adhesion between the probe tip and sample was not considered in these studies. What’s more, sinusoidal signal generator is needed to cause the flexural oscillation of the cantilever. Some other similar studies employed shear modulation spectroscopy [41] and magnetic bead manipulation [42] to obtain the micro/nano viscoelastic properties. All those studies mentioned above measured the dynamic viscoelastic response of materials. By contrast, the methods for assessing the transient viscoelastic response of materials were also proposed. [43-45] They were all founded based on the functional equation methods proposed in the mid of the 20th century [46]. They utilized indenters of different tip geometries and obtained the elastic moduli and viscosity, respectively, based on the viscoelastic contact theories developed from the functional equation method.

With the knowledge about the TMV superlattice and previous methods for mechanical characterization of TMV and TMV-based materials, this thesis will focus on the nanomechanical characterization of TMV superlattice. Not only will the mechanical properties of TMV superlattice be focused, but also the improvement of the conventional methods and proposal of new methods will be concentrated for more accurate results and economic operation. The Atomic Force Microscopy (AFM) is an important experimental tool in our research. AFM is capable of performing *in vivo* measurements on micro/nano materials with high precision in force and displacement probing. A better understanding of the running principle and advantages of AFM, can be obtained from Chapter 2 in this thesis. Chapter 3 and Chapter 4 will introduce our methods to measure the elastic modulus and viscoelasticity of TMV superlattice, respectively. The methods stated there include both the experimental set-up and theoretical derivation for numerical processing. Some fundamental theories of the characterization methods were included in chapter 2, such as the elastic contact mechanics models where the nanoindentation analysis is rooted and viscoelastic theories which serve as a foundation for the new method established in chapter 4. Finite element simulation is a widely used method for mechanical problem. It is able to work as an effective way to confirm the accuracy of the newly develop mechanical testing methods and exhibit the deformation status of nanomaterials which is very difficult to observe. However, the applicability of this method for nanomechanical problems is greatly challenged because the assumption of continuum medium based on which finite element method is formulated may not hold when it is scaled down to nanometer. Then in Appendix, the minimum sizes for finite element is quantitatively studied, based on previous research on the minimum representative volume element sizes for polycrystals and composites. After that, the finite element model for contact system and adhesive forces generated in nano-contact system was developed and analyzed. Then the finite element simulation of AFM-based nanoindentation was performed. The mechanical characterization results based on finite element simulation was compared with the analytical methods proposed in chapters 3 and 4. Finally, in Chapter 6, as a closing, future work is proposed in order to further improve the current research and lead us to better understanding the nanomechanical issues.

CHAPTER 2. LITERATURE REVIEW

This chapter focuses on three subjects.

1) The Atomic Force Microscopy (AFM) methods for mechanical characterization. This part presented the history and set-up of AFM so that readers can be equipped with the necessary knowledge to understand how the AFM works in the elasticity and viscoelasticity measurement in chapter 3 and chapter 4. Besides, some AFM methods available for characterizing elastic modulus, Poisson's ratio, frictional coefficient and some other properties were also introduced, which makes readers be able to realize how the novel methods introduced in the subsequent chapters contribute to the using of AFM.

2) Contact mechanics models. This part sketched the physical foundation based on which those models were developed and the differences between them. Specifically, an adhesion map was included which tells the applicability of those different models. Some of these models will be employed in the following chapters to extract the mechanical properties of sample from AFM-based experimental data.

3) The theories of viscoelasticity. This part started from an introduction to the viscoelasticity, which included how it exists in the nature and the factors that can influence the viscoelasticity. Following that, the conventional methods to measure the viscoelasticity of bulk materials were introduced, including the transient method and dynamic method. The knowledge presented in this part can assist the readers in better understanding the principle behind the novel method proposed in chapter 4 to measure the viscoelasticity as well as how it is different from previous methods.

2.1. AFM methods for mechanical characterization

2.1.1. Introduction to the AFM

The AFM was brought into being in 1986 by three scientists, Binnig, Quate and Gerber, as a powerful tool for surface imaging, force measuring and nano-manipulating [47-49]. Before that, the scanning tunneling microscope, from which AFM was developed, had been invented by Gerd Binnig and Heinrich Rohrer. They were awarded the Novel Prize of physics in 1986 for their invention of the scanning tunneling microscope. Three years after that, the AFM became available commercially and since then tremendous progress in both the application exploration and the device itself has occurred.

The tip of the AFM, mounted at the end of a cantilever, is of great importance for imaging and force sensing. The tip is typically made of silicon or silicon nitride for imaging and indentation on soft biomaterials. For scratching or indentation on hard surface, diamond tip can be employed. To make a better use of the contact mechanics theories, the tip is mostly fabricated with a radius of curvature ranging from 8 nm to several micrometers. More details about the contact mechanics theories for indentation analysis use will be elaborated in the following section. When the tip is involved in the interaction with samples for imaging, the tip will travel along the plane with the height being sensed by the deflection of the cantilever. As shown in Fig.2.1, a laser spot reflected by the back side of the tip serves as a precise tool of detecting the deflection of the cantilever. During an indentation process, the deflection of cantilever becomes an important and reliable method for sensing the indentation force, based on the fact that the cantilevers were specifically designed, fabricated and confirmed to be regarded as a spring.

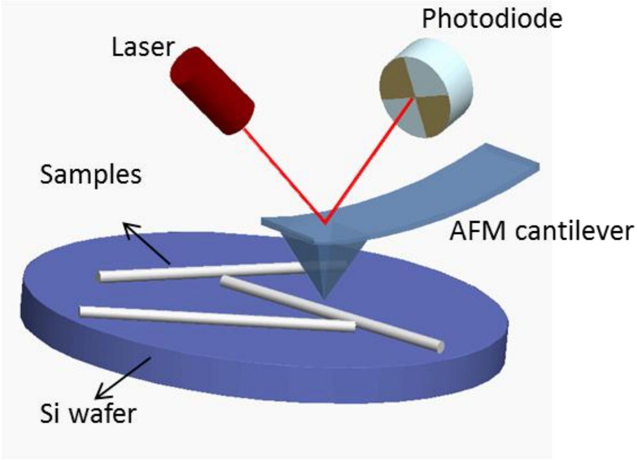

Figure 2.1. A schematic of imaging/indentation by the AFM tip.[50]

By comparison with traditional optical microscopy and state-of-art electron microscopy, the AFM has some intriguing advantages. First, the AFM touches the sample surface to image its topography instead of using light or electron diffraction. As a result, there is no need of any special treatment for the specimen before scanning and the sample can be imaged in ambient air or even liquid which makes it possible to image and characterize biological tissues in-vivo. Second, the very precise control and sensing by piezoelectric and laser-photodiode units enable the AFM to measure force with the precision of 1 pN [51]. Such a feature lends it the feasibility to characterize the mechanical properties of materials in nanoscale or even measure the unfolding force of a single protein molecular as well as the intermolecular adhesion. In principle, the AFM can achieve an atomic level resolution, which is higher than the scanning electron microscope. Besides, some types of AFM can be easily attached with some other accessory devices, such as a micro/nano tensile tester, to extend the utility of the AFM.

In this section, different methods for investigating the mechanical properties of materials with the AFM are summarized. The mechanical properties involved include the elastic modulus, viscoelasticity, hardness and Poisson's ratio. The work by Cappella *et al.* in 1999 initiated the widespread use of the AFM in this regard [52], where the analysis of force distance curve and its use for measuring Meniscus force, Coulomb force, Van der Waals force Double-layer force, Solvation forces, Hydration forces, Hydrophobic force, Steric, depletion, and bridge forces were covered [51]. Since then, quite a number of efforts have been made to determine the mechanical properties of materials in micro or even nanometer scale under the AFM. To sum up, both the experimental setup and theoretical models raised are addressed in this paper. The pros and cons of each method or model are analyzed so that a better understanding of their applicability can be obtained. The problems remaining to be solved are also touched.

2.1.2. AFM methods for elastic modulus measurement

Traditionally, elastic modulus of a material is measured by a tensile test, where the slope of the linear portion of the stress-strain curve represents the elastic modulus. However, such a method is not applicable for nanomaterials, such as biological cell and carbon nanotube, or the micro/nano-scale area of materials, like the interphase area of fiber and matrix of fiber composites. In 1992, an influential work by Dr. Oliver and Dr. Pharr employed nanoindentation technique to extract materials elastic modulus from the indentation load-displacement curve [53]. Even though this method cannot be used directly on AFM because of the difference between the AFM and the nanoindenter, it sparks the idea that AFM-based nanoindentation can be utilized to determine the elastic modulus. All the following elastic modulus determination methods are based on the nanoindentation experiment.

There are two imaging modes commonly used, tapping mode and contact mode. Different probes as shown in Fig.2.2 should be adopted for different modes. For indentation use, tapping mode is usually selected. Before indentation, the topography of the sample surface is supposed to be obtained in order to locate the sample or the area ideal for performing indentation. After that, the scanning area is reduced step by step. It is noted that the ideal indentation spot should be of the largest height and of flat surface. The highest spot, or in other words the thickest place, can protect the tip from pressing down to the substrate large hardness. The contact mechanics theories make more sense for indentation on a flat surface.

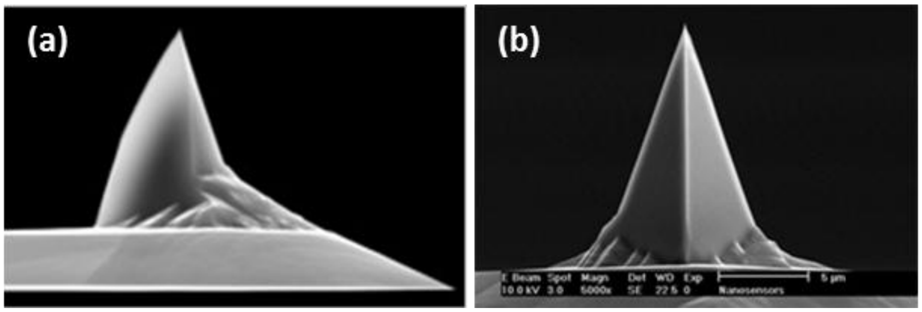

Figure 2.2. (a) AFM tip probe for tapping mode; (b) AFM tip probe for contact mode.[54]

When the scanning size reaches 1×1 nm^2, indentation can be performed after appropriately setting indentation parameters, including the lift height, the indentation depth/the largest indentation load and scan rate which defines the loading/unloading velocity. When the indentation is done, an indentation force-displacement curve is generated. An indentation on substrate which features a very large elastic modulus is performed subsequently which serves to correct the sensitivity of the cantilever. Since the substrate is hard, when the tip is press down to the substrate, it is reasonable to ignore the deformation of the substrate and thus all the displacement during indentation comes from the deflection of the cantilever. The sensitivity here means the ratio of the Z motion of the piezo to the cantilever deflection, which is easily affected by the position of the laser spot on the cantilever, the position of the cantilever in its holder as well as the variation from cantilever to cantilever.

After obtaining the force *v.s.* displacement curves, a variety of contact mechanics models, including Hertz, JKR, and DMT and so on, can be employed to extract the elastic modulus. The introduction of those contact mechanics models and their applicability are stated in the section 2.2.

2.1.3. AFM methods for Poisson’s ratio measurement

Poisson’s ratio is a very important mechanical property which correlates the strains along different directions. However, it’s difficult to measure it, particularly in micro/nanoscale. As a result, very few studies have been reported on how to measure the Poisson’s ratio of micro/nano materials. One study was published to measure Poisson’s ratio specifically of ultrathin polymeric films [55]. Besides of the AFM, a tensile tester is also needed to impose tension on the film so that an *in situ* tensile test can be performed under the AFM. The basic idea utilized in this work is to obtain the deformation vector of a specific line segment on the scanned images before and after the tensile test. The schematic of the *in situ* tensile test under an AFM is displayed in Fig.2.3.

The method stated above is just applicable to a thin film and the surface area of the film should be large enough to be scanned and find a segment. The method to measure the Poisson’s ratio to be introduced below has a wider range of applicability. Technically in this method, the dimension of the samples can be as small as tens of nanometers.

2.1.3.1. Experimental setup

Atomic force acoustic microscopy (AFAM) is needed in this method. AFAM is a kind of contact-resonance AFM, which has the vibration of the cantilever involved. In order to active the vibration of the cantilever, a piezoelectric transducer is designed to generate shear or transverse vibration of the sample put on it. The work flow of AFAM can be found below.

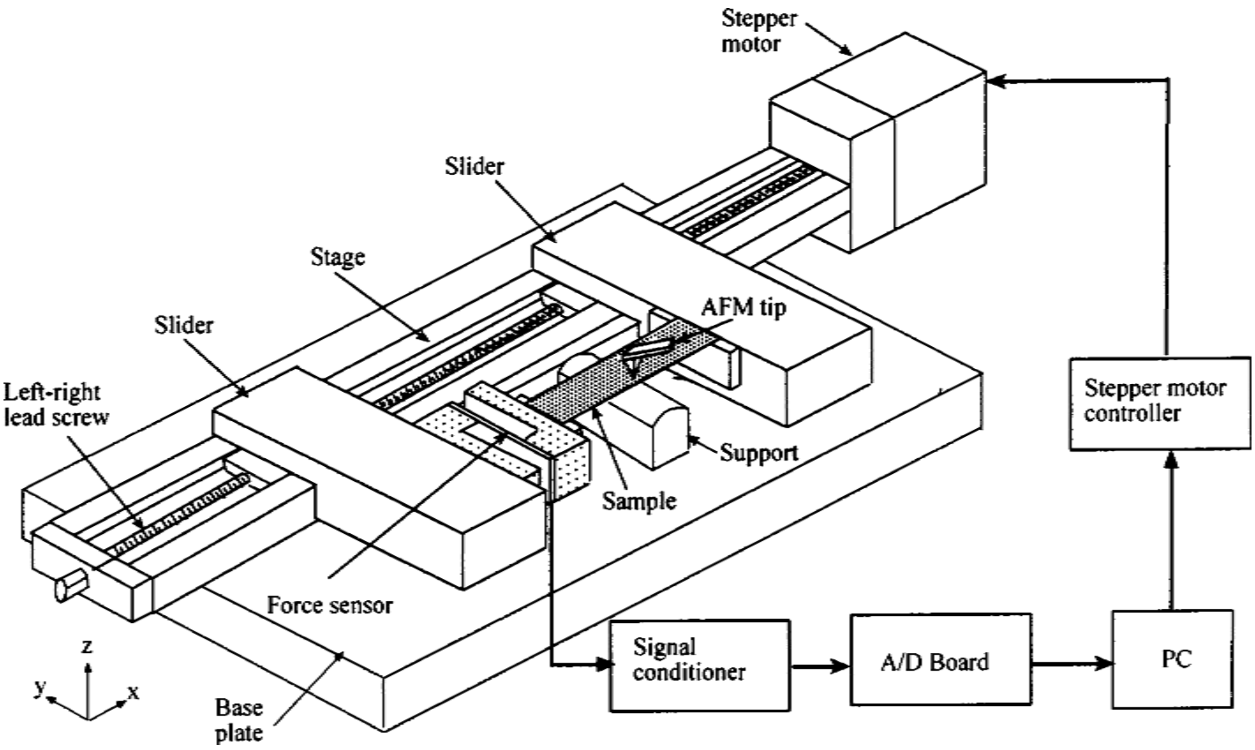

Figure 2.3. Schematic of the in situ tensile test under an AFM.[55]

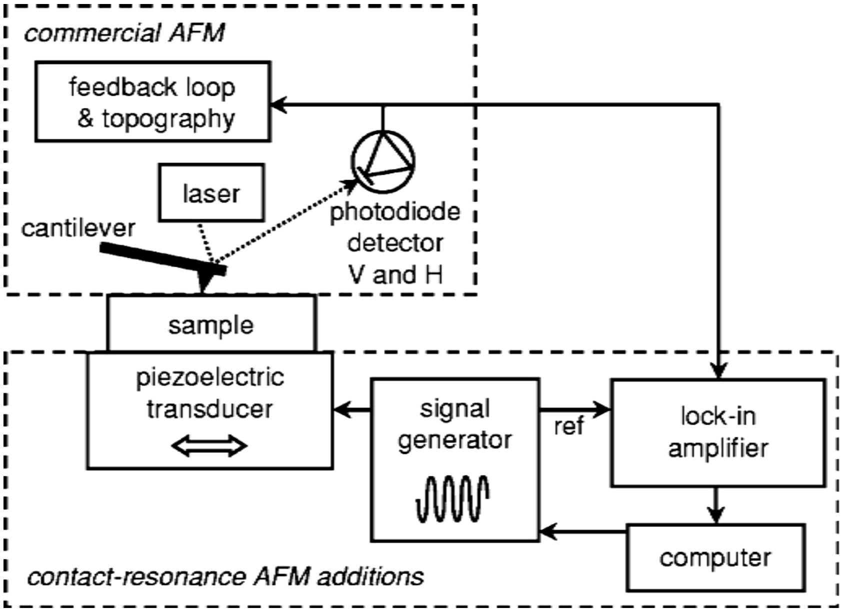

Figure 2.4. Work flow diagram of AFAM.[56]

2.1.3.2. Theoretical formulation

To quantitatively describe the dynamic contact between the AFM tip and the sample, two springs are used to represent the elastic interaction between the tip and the sample along the vertical and the horizontal directions, respectively. The two springs essentially denote the elastic response of the sample. A schematic of the tip-spring model can be found the Fig.2.5. At the same time, the cantilever is also treated as a spring with the flexural spring constant $k_{lever} = \frac{Eb^3w}{4L_1^3}$ and the lateral spring constant $\kappa_{lever} = \frac{Gb^3w}{3Lh^2}$. In the two equations, E and G are the Young's modulus and the shear modulus of the cantilever, respectively; w is the width of the cantilever; h, L and L_1 represent different geometrical parameters of the cantilever as shown in Fig. 2.5. Then the cantilever-spring interaction model becomes spring-spring model. The spring-spring system undergoing vibration has been analyzed in good details in previous literatures. Based those previous works, both $\frac{k}{k_{lever}}$ and $\frac{\kappa}{\kappa_{lever}}$ can be obtained. Thus the vertical spring constant k and the horizontal spring constant κ of the sample can be obtained. Our following discussion to obtain the Poisson's ratio of the sample will be based on the obtained k and κ.

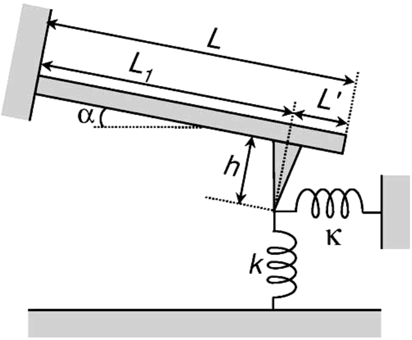

Figure 2.5. Cantilever-spring model.[56]

Attention was first paid to the vertical spring with the spring constant k. k and the nominal elastic modulus of contact couple, E^*, can be related by the following equation.

$$k = 2aE^* \tag{2.1}$$

where *a* is the contact radius and E^* can be calculated from the elastic modulus *E*, and Poisson's ratio *v*, of the sample and the tip, respectively by

$$\frac{1}{E^*} = \frac{1-\nu_{tip}^2}{E_{tip}} + \frac{1-\nu_{sample}^2}{E_{sample}} \tag{2.2}$$

For simplicity, a new parameter $M = \frac{E}{1-\nu^2}$ is defined as the indentation modulus. Thus

$$\frac{1}{E^*} = \frac{1}{M_{tip}} + \frac{1}{M_{sample}} \tag{2.3}$$

Hertz contact model gives rise to the following equation

$$a = (\frac{3RP}{4E^*})^{\frac{1}{3}} \tag{2.4}$$

where R is the radius of curvature of the tip with the assumption that the sample surface is flat so that its radius of curvature can be regarded as infinite; P is the applied force between the tip and the sample.

Invoking equation (2.1) into equation (2.4), we can have

$$k = 2(\frac{3RP}{4})^{\frac{1}{3}}(E^*)^{\frac{2}{3}} \tag{2.5}$$

The same tip and the same contact load were used to perform indentation on a reference sample with a known elastic modulus and Poisson's ratio and perform a second indentation on the sample that we are investigating. The following relationship rises

$$\frac{E_s^*}{E_{ref}^*} = (\frac{k_s}{k_{ref}})^{\frac{3}{2}} \tag{2.6}$$

In the equation above, there is only one unknown parameter E_s^*, thus it can be calculated. After obtaining E_s^*, returning to equation (2.3), give rise to the value of M_{sample} .

The tangential contact involving the tangential contact spring constant κ will then be analyzed. Similar to equation (2.1), κ and the nominal shear modulus G^* can be related by

$$\kappa = 8G^*a \tag{2.7}$$

where the nominal shear modulus

$$1/G^* = (2-v_{tip})/G_{tip} + (2-v_{sample})/G_{sample}, G = E/(2(1+v)).$$

The indentation shear modulus N is defined as $N = \frac{G}{2-v}$ and the following equation can be got

$$\frac{1}{G^*} = \frac{1}{N_{tip}} + \frac{1}{N_{sample}} \tag{2.8}$$

$$\frac{G_s^*}{G_{ref}^*} = \left(\frac{\kappa_s}{\kappa_{ref}}\right)(\frac{k_s}{k_{ref}})^{\frac{1}{2}} \tag{2.9}$$

Though similar procedures aforementioned, the value of G_s^* and therefore the value of N_{sample} can be obtained from Eq.2.8.

By manipulating the equations $N = G/(2-v) = E/[2(1+v)(2-v)]$and $M = E/(1-v^2)$, the expression for Poisson’s ratio can be derived as

$$v = \frac{M_{sample} - 4N_{sample}}{M_{sample} - 2N_{sample}} \tag{2.10}$$

2.1.4. AFM methods for measuring coefficient of friction

Coefficient of friction is a very important mechanical property for components in contact and relative movement. Measuring the coefficient of friction of micro/nano-scale objects, such as micro-electromechanical systems, are possible now with the advent of the AFM. The measurement can be achieved by the AFM-based scratch test on the surface of the sample. The wear mechanism and friction of ultrathin film is of great importance and thus the investigations on it can have lots of applications, for example, magnetic storage devices [57] and artificial biodegradable membrane used in human joints.

Scratching can be performed by applying a ramp load on the tip and then moving the tip along a direction. At the same time, the ramp load and the frictional signal, which are usually recorded in the form of voltage, can be obtained. For samples like biomaterials and other soft materials, a square pyramidal tip fabricated with silicon nitride was adequate enough to perform scratching. The tip has a radius of curvature of tens of nanometers (20-50 nm commonly) and a spring constant of 0.5 N/m at normal load. To perform scratching on hard samples, a three-sided pyramidal tip micro-fabricated with single-crystal diamond is needed. The tip has a radius of curvature as small as 40 nanometers and is mounted on a stainless cantilever with a relatively large spring constant, ~25 N/m. The large spring constant can make the probe undergo a large scratching drag force so that the tip can work well on a hard surface. In scratching/wear test, the tip should be installed on the cantilever in the way that one of its sharp edges goes parallel with the longitudinal direction of the cantilever. Subsequently, the tip will scan on the sample in the transverse direction of the cantilever. Such a configuration simplifies the measurement of friction sensed by the tip. Besides, the repeated tests can be easily performed. It has also been confirmed that the wear when the tip is scanning in the longitudinal direction is 2~3 times larger than that during the tip travels in the other way. The scanning rate for the wear/scratching test is usually set to be 0.5 Hz.

The parameters set for most cases can be found in the following table.

Table 2.1. Parameters selection for AFM-based scratching test[57]

Parameters	Scratch length (μm)	Scanning velocity (μm/s)	Number of loading steps
Value	25	0.5	500

An example of AFM-based scratching experiment performed on a polymeric magnetic tape. Different scratching loads (ramp loads) were used and as a result the scratching depth went linearly with the ramp load (40~140 μN), which can be found in Fig.2.6(a). Then the ramp load was kept constant while different scanning velocities (1~100 μm/s) were applied to the scratching test, which can be found in Fig.2.6(b). The scanning velocity is found to take no effect on the scratching depth and coefficient of friction.

Figure 2.7 demonstrates the determination of the frictional coefficient and the critical load based on AFM-based scratching test. The tip was defined to scratch up to a length of 25μm at the scratching velocity of 0.5μm/s. The ramp load increased gradually with the scratching proceeding. The coefficient of friction remained at 0.04 before the ramp load reached ~35 μN. The ramp load of 35 μN is the critical load in this case. After the critical load, the frictional coefficient kept rising. Then we can conclude that the frictional coefficient between the sample and the AFM tip is 0.04. The critical load represented the load that initiated the plastic deformation of the sample, which can be seen as the scratches on the height image scanned by AFM in Fig.2.6(c). Thus the frictional coefficient after the critical load on Fig.2.6(b) is not the actual value.

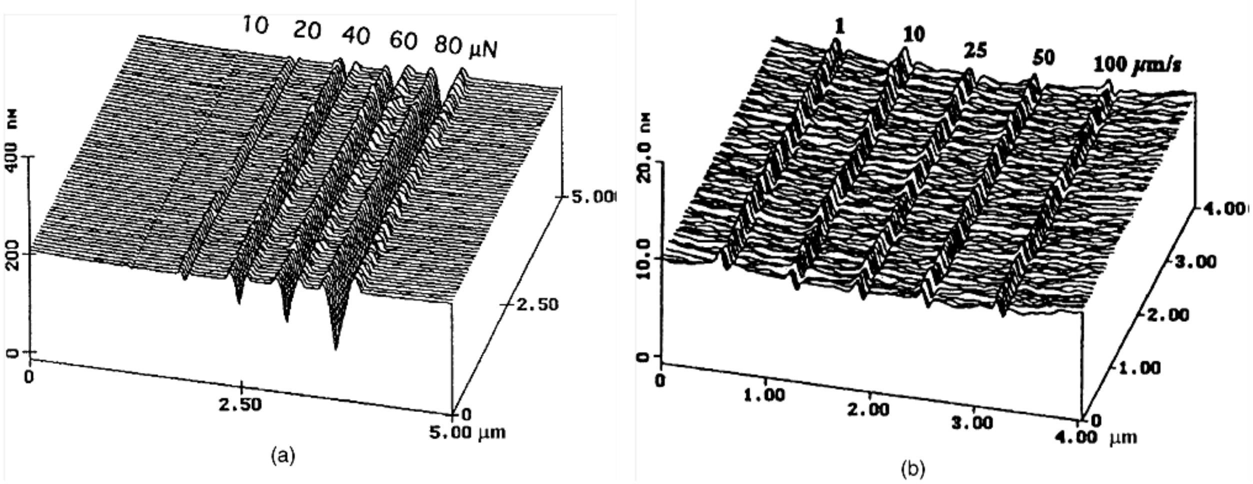

(a) (b)

Figure 2.6. Topography scanned under AFM for (a) Scratches with different loads at the scanning velocity of 2 μm/s; (b) Scratches of the same surface with the same scratching load of 80 μN at different velocities.[57]

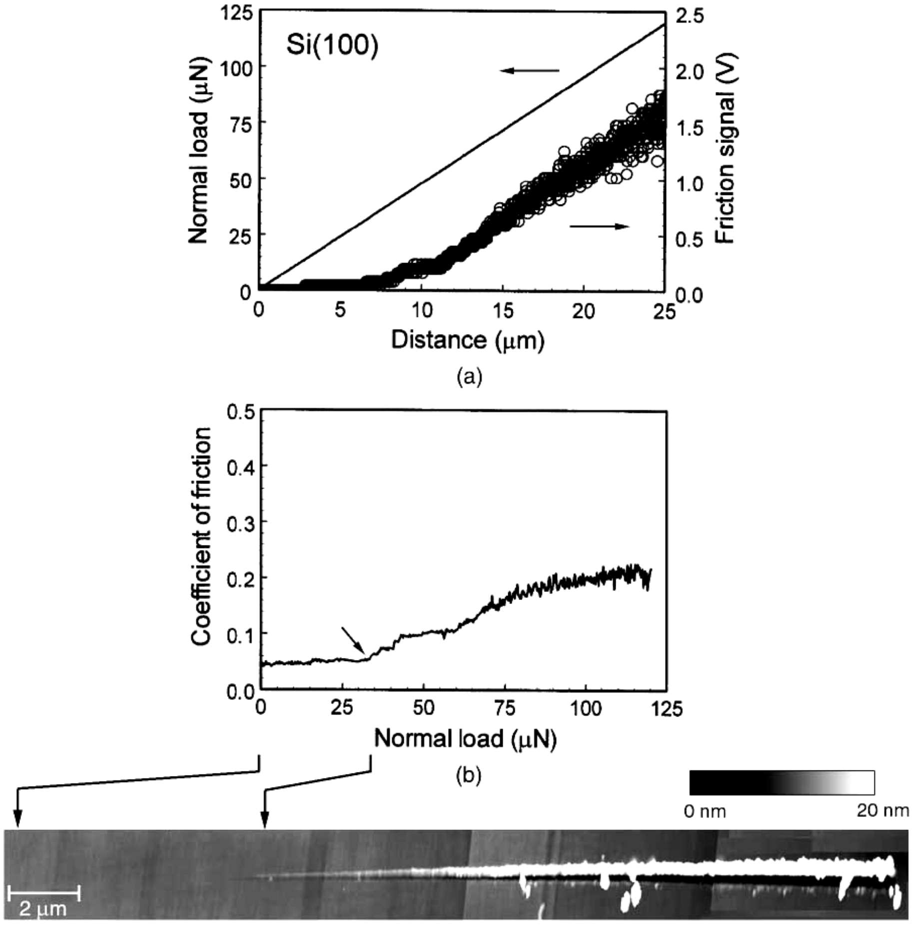

(a)

(b)

(c)

Figure 2.7. (a) Plot of increasing ramp load versus scratching distance as well as the friction signal recorded; (b) Coefficient of friction calculated based on data on (a) versus the ramp load; (c) Height image of scratched surface scanned by AFM.[57]

2.1.5. AFM methods for measuring other mechanical properties

Besides the mechanical properties stated above, some other mechanical properties can also be characterized by the AFM. Hardness can be tested though the same procedures as the macro-scale indentation. The AFM-based indentation has been introduced before. Then the hardness can be obtained by dividing the indentation load with impression area left on the indention surface. However, the hardness has been related to the indentation load-displacement curves, contact depth, Young's modulus, initial yield strength and work-hardening exponent [58]. The details of the relation between the hardness and the other mechanical properties can be found in previous literature[58].

AFM was also utilized to investigate the interfacial mechanical properties of composites [59]. The sliding interfacial strength (also known as friction strength) can be obtained by the following equation,

$$\tau_f = \frac{P^2}{4\pi^2 u r^3 E_f} \tag{2.11}$$

where$u$ is the displacement of fiber generated during indentation, P is the indentation load, r and E_f are the radius and the Young's modulus of the reinforcing fiber, respectively.

The interfacial fracture strength can be obtained by the equation as follows,

$$\tau = \frac{P}{2\pi r t} \tag{2.12}$$

where t is the thickness of the reinforcing fiber. For more details about the experimental and analysis procedure, please look into the reference.

2.2. Elastic contact mechanics models

2.2.1. Hertz model

Hertz model was originally proposed by Hertz in 1986 for non-adhesive elastic contact between two spheres. A very important assumption for this model is that it applies to small contact case where the contact radius is much smaller than the radii of the two elastic spheres. The assumption is resulted from the approximation that the sphere profile was replaced by a parabolic equation for the ease of mathematical derivation [60]. The Hertzian theory for two-sphere contact can be expressed as [61, 62]

$$a^3 = \frac{3\pi}{4}(k_1 + k_2)\frac{R_1 R_2}{R_1 + R_2}P \tag{2.13}$$

$$\delta^3 = \frac{9\pi^2}{16}(k_1 + k_2)^2 \frac{R_1 + R_2}{R_1 R_2}P_?^2 \tag{2.14}$$

where$a$ is the contact radius, $R_1$and R_2denote the radii of the two contact spheres, $k_1 = \frac{1-v_1^2}{\pi E_1}$, $k_2 = \frac{1-v_2^2}{\pi E_2}$, $v_1, ?v_2$ and $E_1 ?E_2$ are the Poisson's ratio and elastic modulus of the two spheres, respectively, P is the contact force, δ is the indentation depth.

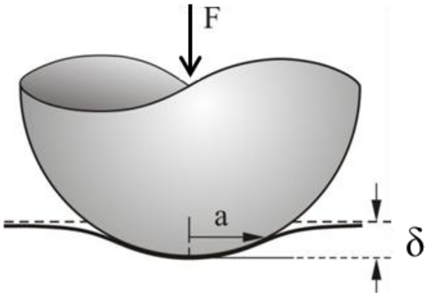

Figure 2.8. Schematic of contact between a sphere and a flat surface.

Hertz model was employed by Wang *et al.* for investigating the elastic moduli of the tobacco mosaic virus and polyaniline fiber, respectively[13]. A similar work by Zhao *et al*. also adopted Hertz model of non-adhesive contact to determine the elastic modulus of single plant virus in tubular shape[36]. The indentation force-displacement curve exhibits that the curve during the retraction of the tip has a portion with negative force before the tip gets out of the contact with the sample surface. The adhesive force is essentially the van der Waals force which exists between molecules and it becomes obvious in the contact between nanometer scale objects. This makes it difficult to fit the experimental indentation force-displacement curve with the Hertz model. The two works aforementioned actually both used the extension curve where the adhesion is minor or even absent and thus can be ignored. Nevertheless, The retraction curves actually tells more information about the elastic deformation than the extension curve which incorporates the plastic deformation component [53]. It was also experimentally demonstrated that the elastic modulus calculated based on the retraction curve is closer to the uniaxial tensile test's results than that from the extension curve [63].

2.2.2. Johnson-Kendall-Roberts (JKR) model

To address this adhesion effect, Johnson-Kendall-Roberts (JKR) model was developed in 1971 [62]. By means of considering the surface energy, the mathematical derivation from Hertz model yields an obvious adhesion. To confirm the correctness of their model, rubber and gelatine surfaces were taken in their contact experiment. In JKR model, the contact circle radius a is related to the applied load Pas

$$a^3 = \frac{R}{K}(P + 3G\pi R + \sqrt{6G\pi RP + (3G\pi R)^2}) \qquad (2.15)$$

where $K = \frac{4}{3\pi(k_1 + k_2)}$ is the nominal elastic constant, G is the adhesion release rate at the contact surfaces,which is determined by

$$G = -\frac{6P_0}{5\pi R} \tag{2.16}$$

where P_0 is the pull-off force.

It is noted that equation (2.16) applies to the displacement-control experiment, which is more stabilized than the load-control experiment [64], and that the energy release rate *G* equals the adhesion energy of the contact area γ in equilibrium system.

Combining equation (2.15) and equation (2.16) yields

$$a^3 = \frac{R}{K}(P - 2P_0 + \sqrt{-4P_0 P + 4P_0^2}) \tag{2.17}$$

The geometrical relationship between *a* and *δ* gives rise to the following equation

$$\delta = \frac{a^2}{R} - \sqrt{\frac{8G\pi a}{3K}} \tag{2.18}$$

Thus, Eq. (2.17) and (2.18) relate the applied force with the indentation depth quantitatively.

2.2.3. Derjagin-Muller-Toporov (DMT) model

Soon after the introduction the JKR model, DMT model was developed which took the surface force out of contact region into consideration [65]. In DMT model, the contact radius and relative approach can be expressed, respectively, as

$$a = [\frac{R}{K}\left(P + 2\pi GR\right)]^{\frac{1}{3}} \tag{2.19}$$

$$\delta = \frac{a^2}{R} \tag{2.20}$$

In contrast to the JKR model, the adhesion release rate is calculated by a different way as follows,

$$G = \frac{P_0}{2\pi R} \tag{2.21}$$

2.2.4. Bradley model

The Bradley model was proposed based on the Lennard-Jones potential which calculates the force between two atomic-scale surfaces by the following equation,

$$P_{LJ} = \frac{16\gamma}{3z_0}[(\frac{z}{z_0})^{-9} - (\frac{z}{z_0})^{-3}] \tag{2.22}$$

where2γ denote the summed surface energy per unit area of the two surfaces, z is the distance between the two planes, z_0 is the equilibrium distance where the potential vanishes.

Applying the relation above, the total force between two rigid spheres with radii of R_1 and $R_2$was derived as [66]

$$P = \frac{16\gamma\pi R}{3}[\frac{1}{4}(\frac{z}{z_0})^{-8} - (\frac{z}{z_0})^{-2}] \tag{2.23}$$

2.2.5. Maugis-Dugdale (MD) model

In order to explain the apparent contradiction between the JKR and the DMT models, MD model was developed in the year of 1991. Instead of using Lennard-Jones potential which may involve self-consistency in numerical calculation, a Dugdale model was used. MD model states that [67]

$$P = \pi w R[\bar{a}^3 - \lambda\bar{a}^2(\sqrt{m^2-1} + m^2\tan^{-1}\sqrt{m^2-1})] \tag{2.24}$$

$$\delta = (\frac{K^2}{\pi^2\omega^2 R})^{-1/3}(\bar{a}^2 - \frac{4}{3}\bar{a}\lambda\sqrt{m^2-1}) \tag{2.25}$$

where m is ratio of contact radius, *a,* and the radius of adhesive region, *c*; *K* is defined in equation (2.15); $\lambda = 2\sigma_0 (R/\pi\omega K^2)^{1/3}$ and σ_0 is the maximum force predicted by equation 2.22; $\bar{a} = a(K/\pi\omega R^2)^{1/3}$.

2.2.6. Adhesion map and applicability of contact mechanics models

The applicability of the contact mechanics models introduced above is important to address so that we are aware of which model should be selected in a specific contact situation. To achieve it, an adhesion map was sketched based on two parameters defined to be $\lambda = \sigma_0 (8R/\pi w K^2)^{1/3}$ and $\overline{P} = P/\pi w R$. Physically, λ is ratio between the elastic deformations to the range of surface forces; $\overline{P}$ measures the ratio between the load and the adhesive force.

Hertz model works well when the adhesion is ignorable by comparison with the load. Mathematically, the condition is

$$\left|\frac{P_a}{P}\right| < \xi \tag{2.26}$$

where *P* is the load and P_a is the adhesive force proposed in the MD model.

The adhesive force can be calculated by

$$P_a = -2\sigma_0 c^2[\cos^{-1}(\frac{a}{c}) + a\sqrt{c^2 - a^2}\,] \tag{2.27}$$

where *a* is the radius of the compression region, c is the radius of the tension region (caused by the adhesion) and σ_0 is the uniform adhesive stress between the region of radius *a* to that of radius *c*.

The value of the parameter hasn't been technically determined so it can be chosen arbitrarily in the range of $\xi << 1$. In Fig. 2.9, the ratio is chosen to be 0.05.

The Bradley model was derived based on the assumption that no deformations occur so this model applies to the case where the elastic moduli of the contact objects are very large. In other words, it applies to rigid contact. The other three models took both the adhesion and the deformation into consideration. However, they are applicable to contacts with different magnitudes of deformation, which is defined by the parameter δ_a / h_0, where δ_a denotes the elastic compression and h_0 is the gap between the surfaces.

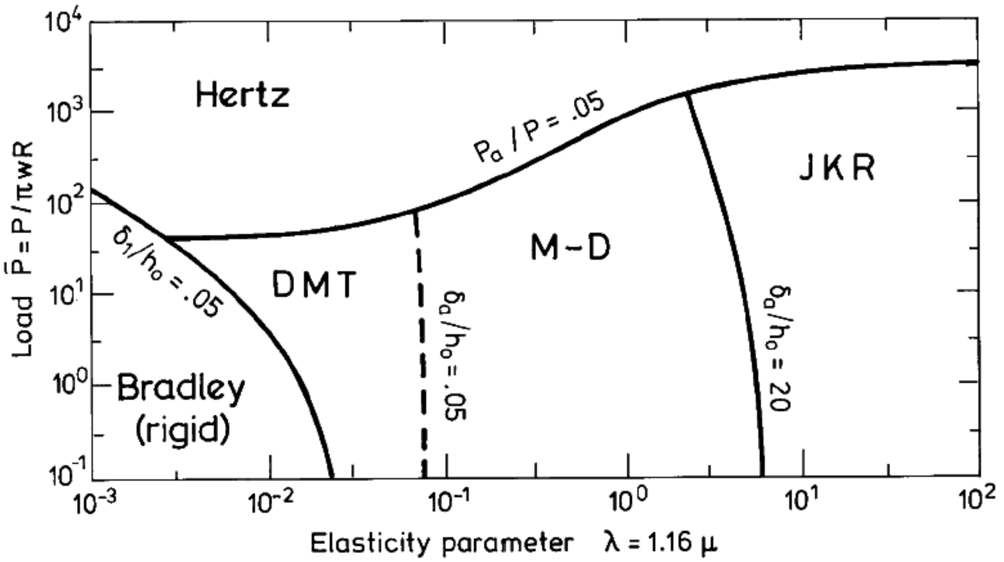

Figure 2.9. Adhesion map for contact mechanics models. [68]

2.3. Theories of viscoelasticity

Most biomaterials, categorized as organic high bio-polymer, exhibit both elastic and viscous behavior. Such mechanical behavior is termed as viscoelasticity. With the involvement of viscous factor which is time/frequency-dependent, the complication of viscoelastic study arises by comparison with studies of pure elastic solids. However, the research on characterizing viscoelasticity has gained much attention in past decades due to its technological significance in physiology, geophysics, and food industry [37].

Not only do the viscoelastic properties change greatly from different types of materials, but also they vary with temperature. Generally, there are three stages for polymers at increased temperature, where the glass-transition temperature, T_g, is of particular importance. When temperature is well below T_g, polymers are elastic solids, essentially an organic glass, with high elastic modulus and time-independent mechanical behavior. When temperature ranges around T_g, viscoelastic behavior dominates. When it's much higher than T_g and reaches beyond the transition range, uncrosslinked polymers behave as a liquid and crosslinked polymers act as elastic solids with very low elastic moduli. Strictly, viscoelastic behavior exists in all materials including those we assume as elastic solids or viscous liquid. Thus, the pure elasticity or viscosity is an approximation in real materials. For more details about the concepts of crosslinked and uncrosslinked polymers as well as the method to determine glass-transition temperature, please refer to reference [69].

2.3.1. Transient experiments for viscoelasticity measurement

Creep and relaxation are the two simplest and widely used transient experiments for viscoelastic measurement. For a creep test, a polymer is subjected to a constant tensile stress, σ_0, it results in a strain, $\varepsilon(t)$, which usually increases with time going by. While for a stress-relaxation test, the strain of a polymer is kept at a specific value, ε_0, the stress applied on it can be recorded as $\sigma(t)$, which degrades with time. Due to the simplicity of experiment, uniaxial tensile test is normally chosen. For a shear-response test, it records a combined behavior of different stresses and thus is more useful than the uniaxial tensile test. Besides, the creep and stress relaxation tests can be done in forms of uniaxial compression, torsion, bending, volumetric compression (under hydrostatic pressure) and some other deformation. Fig.2.10 demonstrates the experimental setup for creep and stress relaxation tests, respectively. In Fig.2.10 (a), the fixture plates and sample should reach thermal equilibrium before the test is run. Then appropriate weights are put on the weight pan to apply a constant shear stress, τ_0 ,to the sample. The position of the movable plate and corresponding time is recorded to obtain the strain history. With the knowledge of the dimensions of the sample, the shear strain response history of the sample, $\gamma(t)$, can be obtained. Therefore, the shear creep compliance of the sample can be calculated through

$$J(t) = \frac{\gamma(t)}{\tau_0} \tag{2.28}$$

The tensile creep compliance can be obtained through similar procedures.

In Fig.2.10(b), the sample is attached to the upper clamp first and the force sensed by the load cell when the sample strip drops down and keep static. Then the sample is attached to the lower clamp which applies a pre-strain to the sample. For the whole measurement duration, the strain of the sample is constant, ε_0, while the stress is decreased, $\sigma(t)$,sensed by the recorder connected to the load cell. The stress relaxation test gives rise to the relaxation modulus by

$$E(t) = \frac{\sigma(t)}{\varepsilon_0} \tag{2.29}$$

Linear viscoelasticity is defined as $J(t)$ is independent of τ_0 and $E(t)$ is independent of ε_0. Hence, the plotting of stress versus strain of linear materials exhibits a straight line, which can serve as an experimental method for judging materials' linearity.

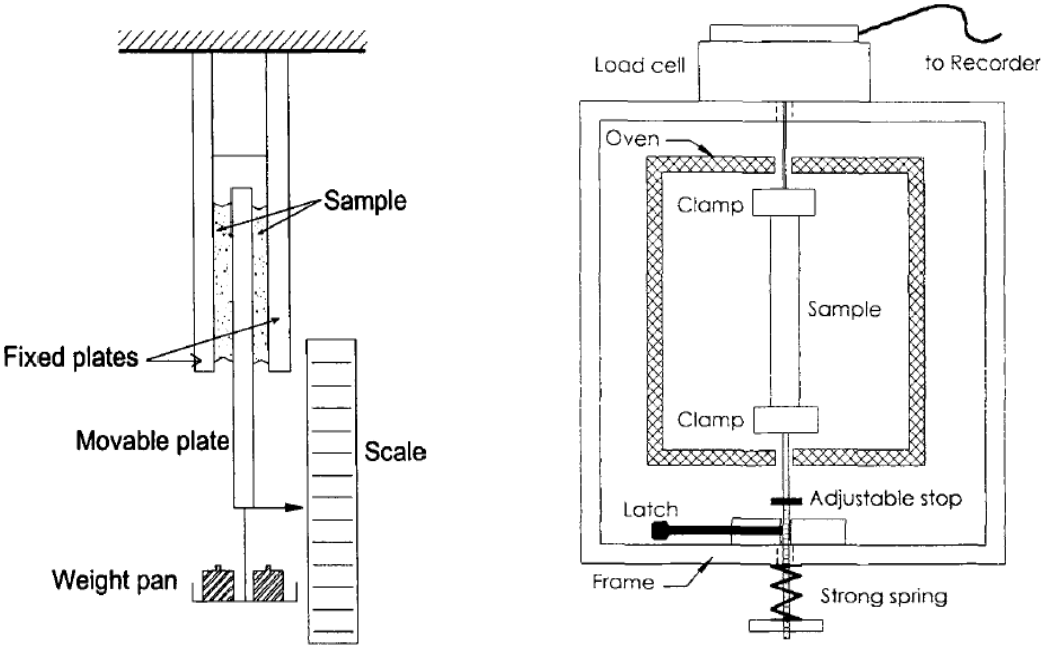

Figure 2.10. (a) An apparatus to measure the shear creep; (b) an apparatus to measure the shear stress relaxation. [70]

2.3.2. Dynamic experiments for viscoelasticity measurement

Besides the transient experiments introduced above, the dynamic experiments to measure the viscoelasticityare also widely used. In a dynamic experiment, the sample is attached to a linear servomotor/electromechanical driver which are able to drive the sample with a sinusoidal strain. On the other end of the sample, a load cell is attached to the sample and records the stress history induced by the sinusoidal strain input. Ideally, the stress signal recorded by the load cell is also in the form of sinusoidal function, as shown in Fig.2.11. If the sample is purely elastic, there will be no phase difference between the strain and stress curves so that they coincide with each other. However, in the case of viscoelastic sample, a phase difference, δ, can be observed. Corresponding to the moment when the strain $\gamma = 0$ and $\gamma = \gamma_0$, the stress sensed by the load cell is signed with σ'' and σ'. σ' is caused by the strain completely (strain rate is zero) so it's an elastic response. σ'' is caused by the strain rate completely (strain is zero) so it's a viscous response. The storage and loss moduli are defined, respectively, as

$$G' = \frac{\sigma_0}{\gamma_0}\cos\delta \tag{2.30}$$

$$G'' = \frac{\sigma_0}{\gamma_0}\sin\delta \tag{2.31}$$

where σ_0 and γ_0 are the amplitudes of stress and strain, respectively; δ is the phase difference between stress and strain.

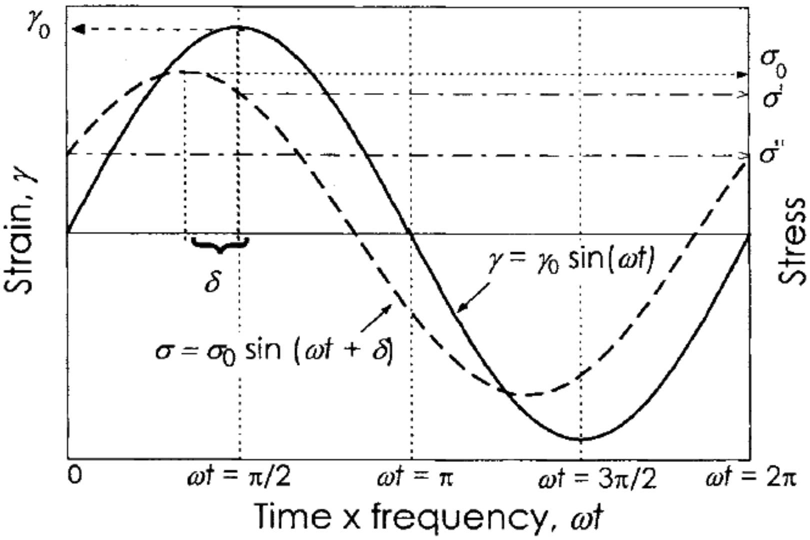

Figure 2.11. Stress of response to a sinusoidal shear in a dynamic test.[70]

By now, two reports on the dynamic experiments for viscoelastic measurement based on the atomic force microscopy (AFM) are available. The first one, published in *Physical Review Letter* by Cappella in 2000 addressed the stress response of oscillation by [38]

$$f_{bead} \approx \frac{4}{3}\sqrt{R}\left(\overline{E}_0\delta^{3/2} + \frac{3}{2}\overline{E}^{*}\sqrt{\delta_0}\,\tilde{\delta}\right) \tag{2.32}$$

where the first term comes from the Hertzian model with zero-frequency indentation and $\overline{E}_0$ is determined by $2G'/(1-v)$; the second term is derived from the oscillation effect and $\overline{E}^{*}$ is determined by 2(G'+iG")/(1-ν); δ, δ_0 and $\tilde{\delta}$ denote the instant indentation, average indentation and oscillation amplitude of indentation, respectively.

The equation above provides foundations to extract the storage and loss moduli from experimental data of oscillatory indentation.

The other article published in the *Journal of Applied Physics*by Oliver in 2008 employed a different philosophy. Contact-resonance AFM was used and the cantilever was excited by a harmonic vibration. The interaction between the tip and the sample surface was approximately formulated with a linear spring-dashpot model. Aided by the elastic Hertz model and the elastic-viscoelastic correspondence principle [71], the storage and loss moduli in terms of reference sample can be determined by [39]

$$G_s^{'} = G_{ref}^{'} (\frac{k_s}{k_{ref}})^m \tag{2.33}$$

$$G_s^{''} = G_{ref}^{''} (\frac{\omega_s c_s}{\omega_{ref} c_{ref}})^m \tag{2.34}$$

whereωis frequency, c is characteristic damping, *k*is the cantilever stiffness, m is a constant depending on the geometries of tip-sample interaction (for spherical contact, m=1.5, and for flat punch contact, m=1), the subscripts "s" and "ref" refers to the sample under investigation and the reference sample.

It is noted that the dynamic experiment for viscoelastic measurement has some constraints. In order to obtain a sinusoidal response of stress, the amplitude of strain applied, γ_0, must be kept small. Otherwise, the stress response will contain some other components which make the stress curve deviates from a sinusoidal function. The larger the strain amplitude is, the more the stress curve deviates from a sinusoidal function. Under certain conditions, the stress sensed by the load cell may even not periodic at all. For example, oscillatory deformation applied on block copolymers can give rise to transient changes in its properties. As a result, chaotic stress signal can even be observed, which makes it very difficult or even impossible to do the analysis on the stress versus strain curves. With those factors taken into consideration, the dynamic experiments do have some shortcomings.

2.3.3. Spring-dashpot model

In order to quantitatively characterize the mechanical behavior of a viscoelastic system, spring-dashpot model have been introduced, where spring denotes the elastic component while the dashpot denotes the viscous component. The model with a spring and dashpot in series is named as Maxwell model. The model with a spring and a dashpot in parallel is named as Voigt model. The model where a Voigt model is in series with a spring is called the standard solid model. A comparison of the three models is displayed in the table below.

Table 2.2. Comparison among different spring-dashpot models

	Maxwell model	Voigt model	Standard solid model
Governing equations	$\dot{u} = \frac{\dot{\sigma}}{G} + \frac{\sigma}{\mu}$	$\sigma = Gu + \mu\dot{u}$	$\sigma + \frac{\mu}{G}\dot{\sigma} = G'u + \mu(1+\frac{G'}{G})\dot{u}$
Creep equations	$u = \frac{\sigma_0}{\mu}t + \frac{\sigma_0}{G}$	$u = \frac{\sigma_0}{G}(1 - e^{-Gt/\mu})$	$u = \sigma_0[\frac{1}{G'} + (\frac{1}{G'+G} - \frac{1}{G'})\exp(\frac{-G'G}{\mu(G'+G)}t)]$
Relaxation equations	$\sigma = \sigma_0 e^{-Gt/\mu}$	$\sigma = Gu_0$	$\sigma = u_0(G'+Ge^{-Gt/\mu})$

Note: *G* represents the elastic modulus of spring, *μ* represents the viscosity of the dashpot, *t* is the variable of time, *u* is the strain and *σ* is the stress.

CHAPTER 3. ELASTIC MODULUS MEASUREMENT OF TMV SUPERLATTICE

This chapter addressed the method for measuring the elastic modulus of TMV superlattice. Both the AFM-based nanoindentation experiment and the numerical procedures were introduced. In addition to elastic modulus, the surface energy density of the sample was also investigated which plays an important role in bio-adhesion. Particularly, the superiority of extended JKR model over the original JKR model was stated specifically for nanoindentation. According to the X-ray analysis which has been covered in the first chapter, the neighboring TMVs were found to be separated by 3.6 nm. This leads us to the guess that the electrostatic force on the surface of TMVs assembles them at such an equilibrium pattern. In order to assess the influence of the electrostatic field to the mechanical properties, finite element simulation was performed where the TMV superlattice was modeled to be a composite structure with tubular TMV being filler and with electrostatic field being the matrix.

3.1. Nanoindentation experiment

The details of TMV superlattice synthesis can be found elsewhere.[21] The TMV superlattice solution was obtained from the mixture of the TMV and $BaCl_2$ solution (molar ratio of Ba^{2+}: TMV = 9.2×10^4: 1) and further diluted with deionized water (volume ratio 1:1). A drop of the diluted solution (10 μL) on a Si wafer was centrifuged at 800 rev/min for 10 s to get mono-layer dispersion. The sample was dried for 30 min under ambient conditions (40% R.H., 21 ℃) for subsequent AFM (Veeco 3100) observation and mechanical testing. The undiluted superlattice sample was also scanned under a field emission scanning electron microscope (FESEM, Hitachi S4700).

The AFM-based nanoindentation was performed under the nanoindentation mode (AFM probe type: Tap150-G, Nanoandmore), shown schematically in Fig.3.1. The AFM silicon probe was measured in FESEM to have a length of 125 µm, a width of 25 µm, and a thickness of 2.1 µm. The tip radius is 12 nm. For a typical indentation test, the tip was pressed into the sample surface for less than 4 nm which is much smaller than the radius of the tip, hence the tip was assumed to have a spherical profile. The indentation was performed at 10 different locations with an indentation speed of 185 nm/s. The neighboring indentation locations were 500 nm apart to avoid the deformation effect to the adjacent indentation. The corresponding reaction force *vs.* Z piezo displacement (F-DISP) curve was recorded. The Z piezo displacement after the tip-sample contact was the combination of the sample deformation (i.e., indentation depth Δz) and the cantilever deflection. To separate the two, indentations were also performed directly on a rigid Si wafer.[13] Thus, the force *vs.* indentation depth (F-Δz) relationship was obtained for elastic modulus analysis.

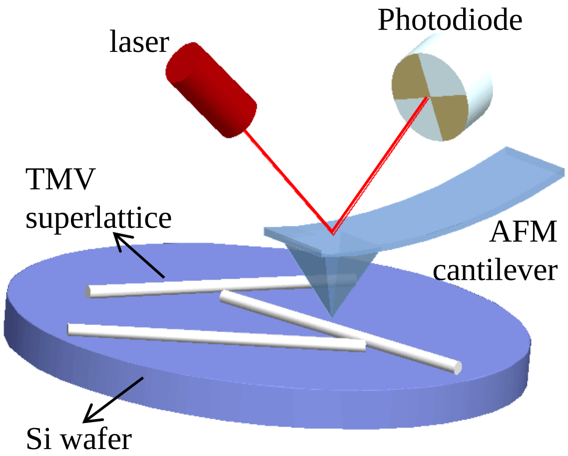

Figure 3.1. Schematic of AFM nanoindentation on the TMV superlattice.[50]

To convert the AFM cantilever deflection to its corresponding reaction force, several methods on measuring the cantilever spring constant k_c have been available, such as the thermal fluctuation measurement method, the kinetostatic method, the heterodyne interferometry method, and the extended added-micro drop method.[72-76] The Sader method [74] was used here:

$$k_c = M_e \rho_c b h l \omega_{vac}^2 \tag{3.1}$$

where M_e, the normalized effective mass, is taken to be 0.242; ρ_c is the density of the Si cantilever; ω_{vac} is the cantilever's unloaded resonance frequency; b, h and l denote the width, thickness and length of the cantilever, respectively.

To investigate the reinforcing effect of the Ba^{2+} to the mechanical properties of the superlattice, a finite element model was built in ANSYS. The TMV superlattice rod was modeled as a composite, with Ba^{2+} taken as the matrix and the TMVs as the fiberfill. The Si wafer was modeled as a rigid surface and the AFM tip as a sphere with the radius of 12 nm. Two contact pairs were used to simulate the indentation process. One was established between the tip and the sample, where the rigid sphere tip was defined to move downward to the superlattice; the other one was between the sample and the rigid surface, where no relative movement took place. By simulating the indentation process, the elastic moduli of both the Ba^{2+} matrix and the superlattice were determined.

3.2. Results and discussion

It is observed from the FESEM image (Fig.3.2(a)) that the rod-like particles are tens of microns in length and several microns in width. Figure 3(b) shows the AFM height image of a representative TMV superlattice rod with a cross-section inset. The superlattice is 19.2 μm in length, and ~300 nm in diameter.

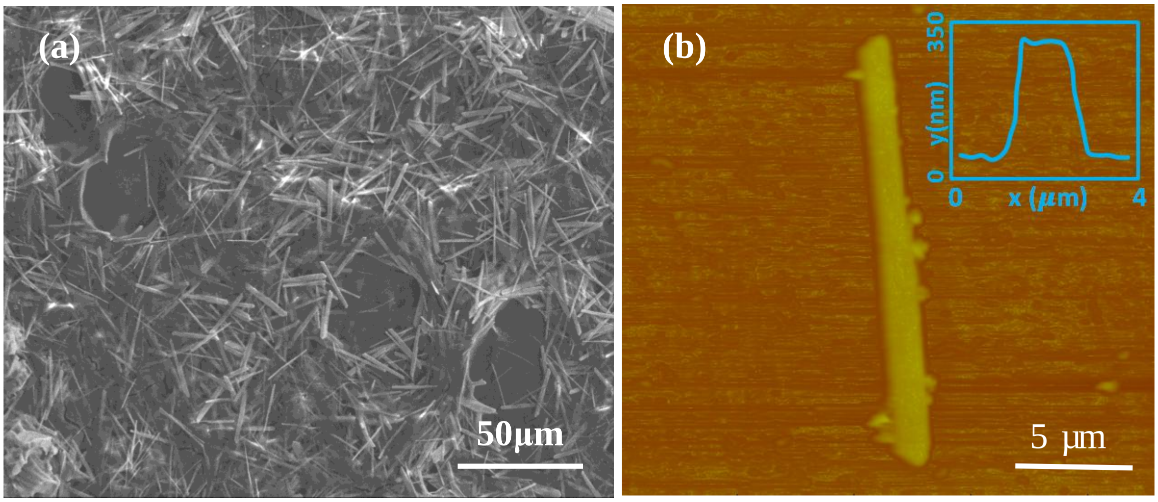

Figure 3.2. (a) FESEM image of the rod-like superlattice; (b) AFM height image of a single TMV superlattice.[50]

Indentation curves were shown in Fig.3.3. It is seen that as the AFM tip approached the sample surface, a sudden drop in reaction force occurred in Fig.3.3(a). The decrease in force was caused by a strong short-range van der Waals attraction between the sample surface and the tip. After the "jump to contact" point, the reaction force increased rapidly as the tip was further pressed down. The F-DISP curves in Fig.3.3indicates that the adhesive force beomes more evident during the retraction. Figure 4(b) exhibites a stronger attraction between the tip and Si wafer. The contact deformation is a well-known nonlinear phenomenon, shown in Fig.4(a), while the the cantilever of AFM probe is designed to behave similar to a linear spring. The difference of the two curves in Fig.3.3 verifies our assumption that the deformation of indentation on the silicon wafer is negligible. As a result, for the retraction curvesof Fig.3.3(a) and (b), the difference in deformation for a specific force, can be regraded as the sample deformation.[63]

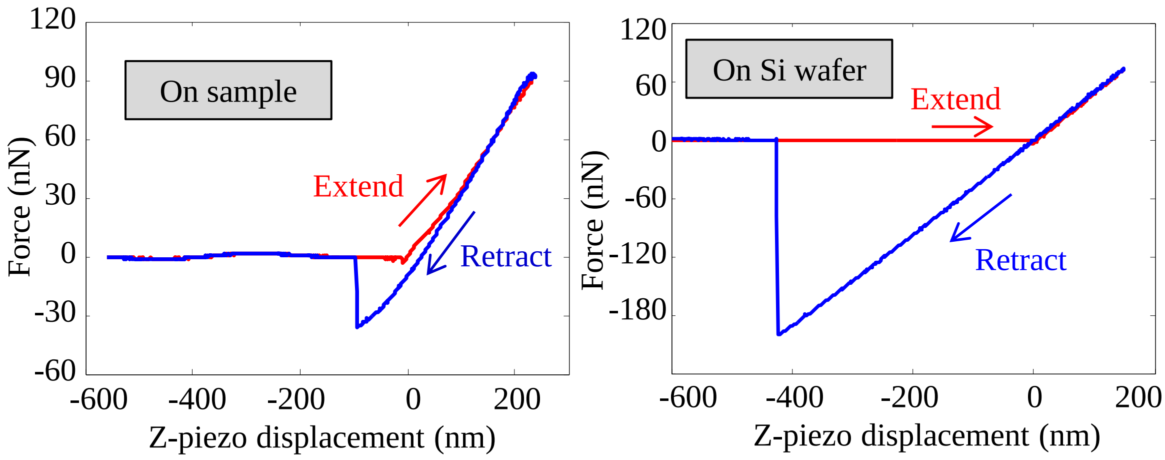

Figure 3.3. F-DISP curve on (a) TMV superlattice and (b) Si wafer.[50]

3.3. Theoretical analysis

Hertz model has been widely used for non-adhesive elastic contact.[13, 36] The adhesion at the nanoscale contact, however, may significantly affect the F-Δz curve, based on which the elastic modulus is determined.[77, 78] To address this adhesive effect, Johnson-Kendall-Roberts (JKR) model and Derjaguin-Muller-Toporov (DMT) model were developed in 1970s.[65, 79] Depending on the Tabor parameter μ ,these two models are applied for two different cases. JKR model is appropriate when $\mu > 10$, while the DMT model is more applicable for situations of $\mu < 0.1$.[68, 80]

However, all the three models are based on the simplification of a spherical profile to a parabola. This geometrical approximation is valid for relatively small contact radius with respect to the radius of spheres in contact. To address large contact radii problems, Maugis*et al.* extended the JKR model by replacing the parabolic equation with a sphere profile.[60] The extended JKR model, which fits well with our case, was used for nanoindentation analysis here.[81, 82]

The indentation depth Δz and the load P for the extended JKR model can be expressed as:

$$\Delta z = \frac{a}{2}\ln\frac{R+a}{R-a} - \sqrt{\frac{8\pi a G}{3K}} \tag{3.2}$$

$$P = \frac{3aK}{2}\left(\frac{R^2+a^2}{4a}\ln\frac{R+a}{R-a} - \frac{R}{2} - \sqrt{\frac{8\pi a G}{3K}}\right) \tag{3.3}$$

where a denotes the contact radius; the nominal elastic constant K is calculated by

$$K = \frac{4}{3\pi(k_1+k_2)} \tag{3.4}$$

where $k_1 = \frac{1-v_1^2}{\pi E_1}$ and $k_2 = \frac{1-v_2^2}{\pi E_2}$, v_1, v_2 and E_1, E_2 are the Poisson's ratios and elastic moduli of the two spheres, respectively; G is the adhesion release rate at the contact surfaces, which is determined by

$$G = -\frac{3P_0}{2\pi R} \tag{3.5}$$

where P_0 is the pull-off force; the nominal radius R is obtained by

$$R = \frac{R_i R_s}{R_i + R_s} \tag{3.6}$$

where R_i and R_s are the radii of the indenter and sample in contact, respectively.

To calculate G , P_0 is calculated to be 16 nN, an average value of 30 indentation results. R becomes $R = R_i = 12$ nm, considering that the top surface of TMV superlattice is flat, with $R_s = \infty$. Thus K is reduced to $K = \frac{4E_2}{3(1-v_2^2)}$. The Poisson's ratio of TMV superlattice is taken as 0.38, a commonly used value for biological materials.

Based on equations (2) and (3), the F-Δz curves of different elastic moduli are plotted in Fig.3.4 (a). It is observed that the non-zero horizontal intercept Δz_0 varies with elastic modulus, indicating that the downward adhesion and upward reaction forces are balanced at a deformation position.

For calculation of the elastic modulus, the experimental F-Δz data is needed to fit to the F-Δz curve predicted by the extended JKR model. The experimental Δz data, shown in Fig.3.4(b), is the horizontal difference between the data of the retraction curves of the sample and the Si wafer (Fig.3.3(a and b)) under the same force. The non-zero Δz_0, which is the horizontal intercept from the model in Fig.3.4(a), remains unknown until the elastic modulus is determined. To determine Δz_0, some available methods have been reported, such as the nonlinear least-square error fitting method.[64, 83, 84] An easy approach is proposed here to avoid the complexity of numerical processing. As for the experimental F-Δz data, the retraction curve for the wafer (dashed line in Fig.3.4(b)) is shifted left (solid brown curve) in order that the points, where the cantilever has no deflection for both curves, overlap. Correspondingly, curves from extended JKR model is also left shifted horizontally in order that they intersect at the origin as shown in Fig.3.4 (c). Then the shifted F-Δz curves of different elastic moduli from the extended JKR model can be fitted with the experimental F-Δz data points which are displayed as the red asterisks in Fig.3.4(c). The best fitting result can be determined by investigating the coefficient of determination (R^2). The best fitted elastic modulus of 2.14 GPa, with R^2 being 0.8730, can be found as shown in Fig.3.4 (c).

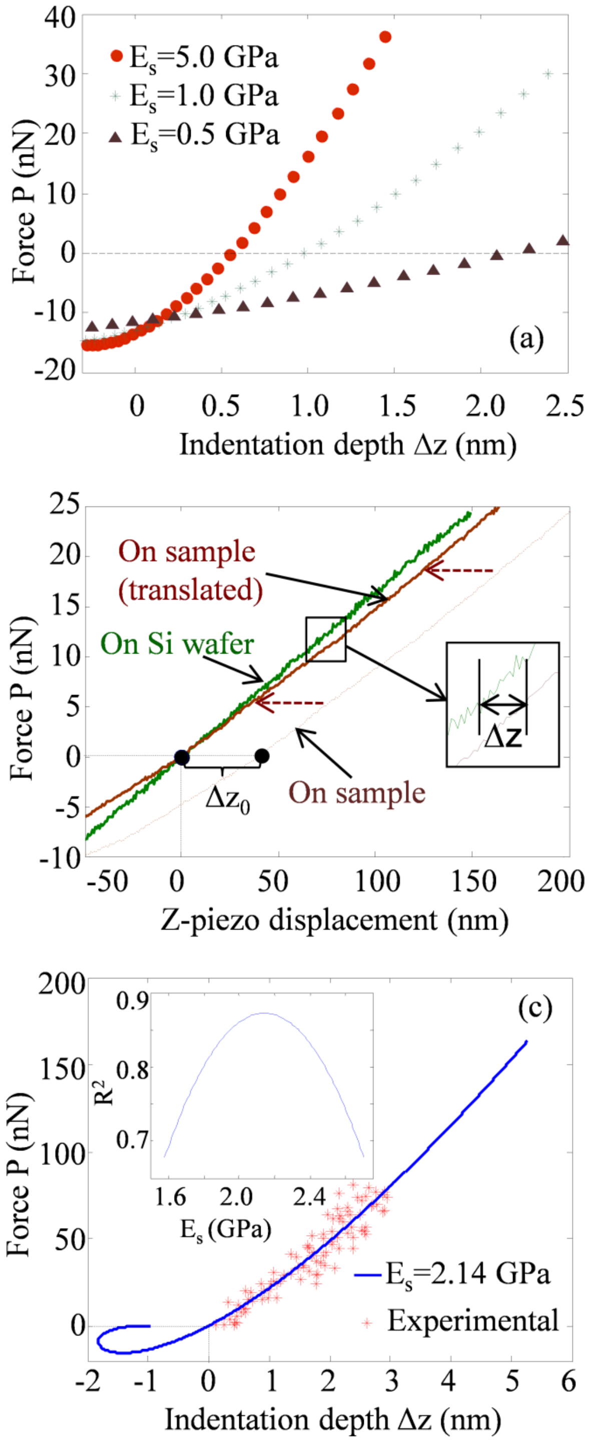

Figure 3.4. (a) F-Δz curves generated from the extended JKR model; (b) F-DISP retraction curves on the Si wafer and shifted sample curve sample; (c) Horizontally translated extended JKR F-Δz curves and experimental results; the inset shows the coefficient of determination.[50]

3.4. Finite element analysis

Finite element analysis (FEA) was conducted to evaluate the reinforcing effect of the like-charge forces between the TMVs and the mechanical properties of the TMV superlattice. The superlattice was assumed to be a composite cylinder structure consisting of 2-D hexagonally packed TMVs and Ba^{2+} matrix filled between the TMVs. The center-to-center distance of the two neighboring TMVs is 21.6 nm[21], and the elastic modulus of TMV is 1.1 GPa [13, 34, 36]. The AFM tip was modeled as a 12 nm-radius sphere. It was noted that the superlattice rod of 1-2 μm diameter contains hundreds of TMVs. For simplicity, a model consisting of 7 TMVs was built. Due to the change of geometry, the experimental F-Δz data could not be applied to the model. Based on the extended JKR model, the corresponding F-Δz relation in the FEA was calculated by adjusting R in equation (2) and (3). The indentation depth of the tip changed from 2.61 nm to 2.88 nm when a force of 40 nN was applied. The adhesive force of 9.72 nN at that point was obtained from the extended JKR and Hertz curves, as shown in Fig.3.5. The total pressing-down force acting between the tip and the sample surface, therefore, was taken to be 49.72 nN.

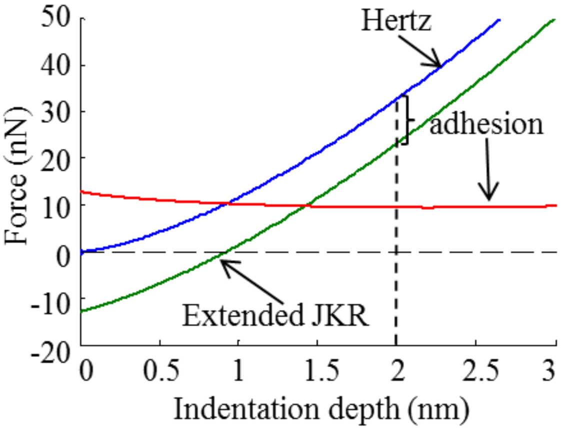

Figure 3.5. Adhesion approximated from Hertz and extended JKR curves.[50]

The elastic moduli of the matrix were found to vary from 3.5 GPa to 10 GPa, as shown in Fig.3.6. The results in Fig.3.6 imply that the fitted elastic modulus of the matrix varies with the indentation locations. The estimated elastic modulus of the matrix essentially shows the mechanical strengthening effect of the like-charge forces between adjacent TMVs. They contribute more on resisting the pressing-down forces than the TMVs to maintain a balanced center-to-center distance between TMVs. Such a strong mechanical reinforcing effect takes responsibility for maintaining the equilibrium distances between TMVs with no regard to the TMV concentration or PH.

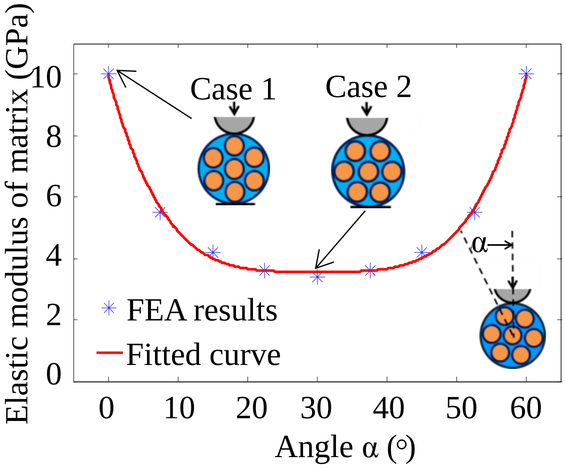

Figure 3.6. Elastic modulus of matrix variation with different indentation locations.[50]

With the Halpin-Tsai model[85], the transverse elastic modulus of the superlattice was determined between 4.38 GPa and 2.00 GPa. This is in a good agreement with the prediction from the extended JKR model. Under an indentation force of 49.72 nN, the von Mises stresses distributions with two cases of indentation locations were presented in Fig.3.7. It is shown that the deformation mostly occurs in the matrix and the TMV tube right below the tip, while the other TMVs are almost not affected. This indicates that, the indentation depth mainly comes from the upper surface of the TMV. Figure 8 also shows that the indentation load was mainly held by the matrix right below the tip, yet the adjacent TMVs had much less reinforcing effect on the whole composite structure. Interestingly, the maximum von Mises stress happens within the matrix, rather than on the surface in contact with the tip. The von Mises stress distribution in both cases indicates that the TMVs have little contribution to the support of the indentation, which suggests the like-charge force is the major components in reinforcing the mechanical properties of the superlattice structure.

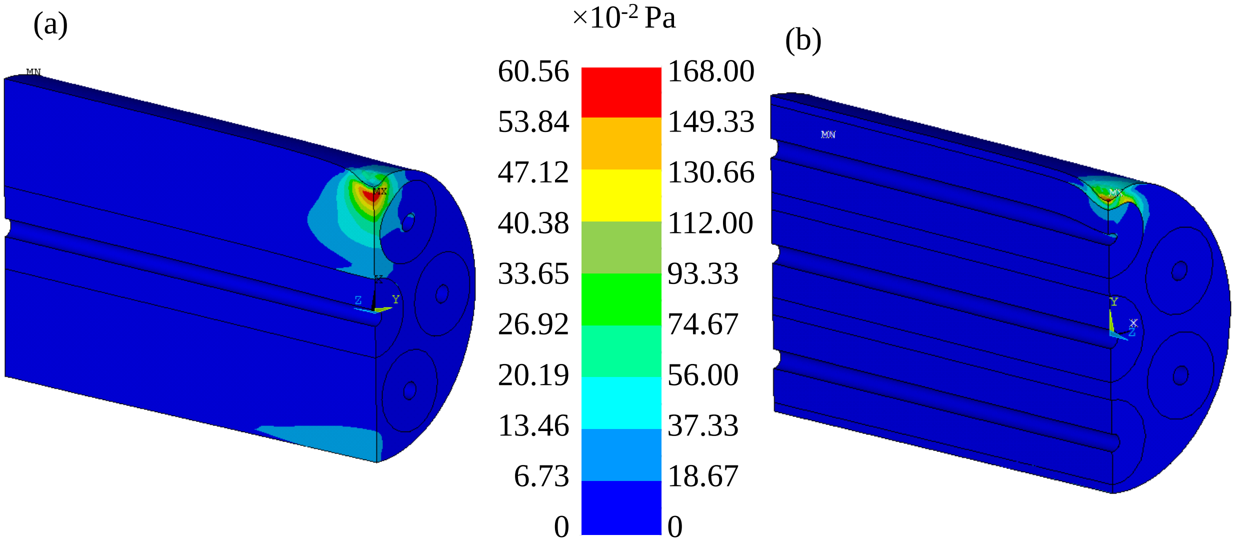

Figure 3.7. Von Mises stress distribution of (a) Case 1 at $\Delta z = 2.81$ nm and $E_{matrix} = 10$ GPa; (b) Case 2 at $\Delta z = 2.85$ nm and $E_{matrix} = 3.5$ GPa.[50]

3.5. Summary

AFM based nanoindentation was employed to evaluate the elastic modulus of TMV superlattice formed by TMV in Ba^{2+} solution. Based on the experimental F-Δz data, the extended JKR model was utilized to extract the elastic modulus of the superlattice. A simple fitting procedure was proposed for fitting the experimental data with the extended JKR model. The elastic modulus was determined to be ~2.14 GPa, which is higher than that of the TMVs. Along with that, the surface energy density of the sample was also obtained, which is ~ 0.6 J/m^2. To further investigate the mechanical reinforcing effect of the charge-like force induced by Ba ions, finite element analysis was then conducted to simulate the indentation, where a series of elastic moduli of the matrix were utilized. The adhesive forces between the tip and the sample surface were included in the simulation. Considering different indentation cases, the transverse elastic moduli of the superlattice were obtained to be in the range of 2.00 GPa and 4.38 GPa. The results show that superlattice has higher elastic modulus than its constituents. The elastic modulus of the TMV superlattice is found to be close to that of wet tendon, and larger than most biomaterials. It was revealed that the like-charge forces play an important role in strengthening the superlattice and thus make it stiffer than TMVs.

CHAPTER 4. VISCOELASTICITY MEASUREMENT OF TMV SUPERLATTICE

To obtain the knowledge of viscoelasticity of TMV superlattice, this chapter presented both the experimental and the theoretical processes to achieve it. At first, the functional equation method was introduced which was employed to extend the elastic contact mechanics model to viscoelastic solution. Then the AFM-based nanoindentation experiment was detailed to demonstrate the transient viscoelastic experiment. Finally, the numerical method for quantitatively characterizing the viscoelastic property was shown. The method described in this chapter provides a new avenue to measure the viscoelasticity of nano-biomaterials.

4.1. Mathematical formulation of viscoelastic system

4.1.1. Functional equation method

Viscoelastic analysis involves both space-and time-dependent factors. In 1955, Laplace transform was introduced into the stress analysis on viscoelastic materials to significantly reduce the complexity generated by the time dependent factors.[86] Moreover, this method extended theories of elasticity that have been accomplished to viscoelastic problems. It has been demonstrated in reference [86] that a unique viscoelastic solution can be obtained by each elastic solution to boundary value and initial value problems. However, this method was limited to the situation where the boundary conditions can be applied to Laplace transform. In realization of this problem, Radok*et al.* extended the applicability of the Laplace transform method to a more general situation by using the approach of functional equation.[46] Recently, the functional equation method has been employed on analyzing flat-punch [43] and spherical-tip indentations[44] of viscoelastic materials, where the indenters are capable of recording the loading and displacement history. In comparison, AFM processes a higher accuracy in force sensing (as small as 1 pN) and displacement sensing (1 nm),but lacks the real-time control of the loading *vs.* displacement of the tip. Thus, the indenter-based indentation methods cannot be utilized for AFM-based nanoindentation on viscoelastic bodies. Besides, the strong adhesion [87] between the AFM tip and the TMV superlattice will significantly affect the determination of the viscoelastic properties. In the following section, we employed the functional equation method to develop a contact mechanics model for indentation on viscoelastic materials with adhesion. Specifically for AFM based nanoindentation, a modified standard solid model was proposed to extract the viscous and elastic parameters of the TMV superlattice.

As a premise of the functional equation method, a quasi-static condition is assumed so that inertial forces of deformation can be neglected.[46, 86]The general constitutive equations for a linear viscoelastic/elastic system in Cartesian coordinate can be written as

$$P^d s_{ij} = Q^d e_{ij} \tag{4.1}$$

$$P^m \sigma_{kk} = Q^m \varepsilon_{kk} \tag{4.2}$$

where s_{ij} and e_{ij} are deviatoric stress and strain, respectively; σ_{kk} and ε_{kk} are mean stress and strain, respectively. The four linear operators P^d , Q^d , P^m and Q^m can be expressed in the forms of

$$P^d = \sum_{i=0}^{N_1} p_{\mathrm{i}}^d \frac{\partial^i}{\partial t^i}\,;\ Q^d = \sum_{i=0}^{N_2} q_i^d \frac{\partial^i}{\partial t^i} \tag{4.3}$$

$$P^m = \sum_{i=0}^{N_3} p_i^m \frac{\partial^i}{\partial t^i}\,;\ Q^m = \sum_{i=0}^{N_4} q_i^m \frac{\partial^i}{\partial t^i} \tag{4.4}$$

where i (i=0,1,2,…) is determined by the selected viscoelastic model; p_i^d , q_i^d , p_i^m and q_i^m are the components related to the materials property constants, such as elastic modulus and Poisson's ratio.

To quantify the viscoelastic behavior, spring-dashpot models have been used as an effective analogy. For a pure elastic system, the model is reduced to a spring only and the linear operators above can be determined to be

$$P^d = p_0^d \, , \; Q^d = q_0^d \, , \; P^m = p_0^m \, , \; Q^m = q_0^m \tag{4.5}$$

According to the elastic stress-strain relations, the elastic linear operators above are correlated as follows:

$$\frac{P^d}{Q^d} = \frac{p_0^d}{q_0^d} = 2G, \; \frac{P^m}{Q^m} = \frac{p_0^m}{q_0^m} = 3K \tag{4.6}$$

where G is the shear modulus, and K is the bulk modulus.

Elastic solutions are sought to obtain the functional equations of nanoindentation on a viscoelastic body. There are a few contact mechanics models available to simulate the indentation process, such as Hertzian theory [61],JKR model [79],DMT model [65] and so on [60, 67, 88]. Detailed comparisons between them and their applicability can be found in chapter 2 and Reference [68]. DMT model was used in this work as a solution for indentation on an elastic body with adhesion.

According to DMT model [65],the indentation load F and relative approach δ can be expressed as

$$F + 2\pi\omega R = \delta^{\frac{3}{2}} E^* \sqrt{R} \tag{4.7}$$

where R is the nominal radius of the two contact spheres R_1 and R_2, given by $R = R_1 R_2 /(R_1 + R_2)$; the adhesive energy density ω can be obtained from the pull-off force F_c, where $F_c = 3\pi\omega R / 2$; the nominal elastic modulus E^* can be obtained from the elastic modulus and Poisson's ratio of the sample by $E^* = 4E_s / 3/(1-v_s^2)$ considering that the elastic modulus of the tip is much larger than that of the sample.

To find the time-dependent relation between the indentation load F and the indentation depth δ, by combining Eq. (4.6) with,

$$G = \frac{E}{2(1+v)},\ K = \frac{E}{3(1-2v)} \tag{4.8}$$

it yields

$$E^* = \frac{4(Q^d P^v Q^d + 2P^d Q^v Q^d)}{3(2Q^d P^v P^d + P^d P^d Q^v)} \tag{4.9}$$

Subsequently, we would first obtain the functional equation of contact radius a *v.s.* indentation depth δ. (The schematic of sphere contact and the physical meaning of parameters can be found in Fig.4.1.)

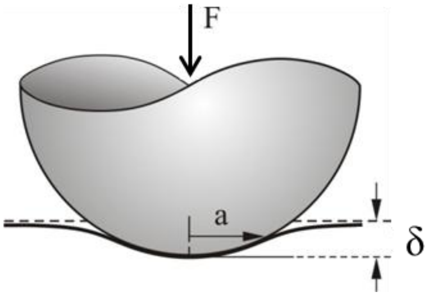

Figure 4.1. Schematic of contact between a sphere and a flat surface.

Invoking Eq. (4.9) into Eq. (4.7), the functional equation is obtained as

$$(2Q^d P^v P^d + P^d P^d Q^v)[F(t) + 2\pi\omega R] = \frac{4\sqrt{R}}{3}(Q^d P^v Q^d + 2P^d Q^v Q^d)[\delta(t)]^{3/2} \tag{4.10}$$

The linear operators need to be determined so that the elastic solution can be related to a viscoelastic solution. As stated before, the viscoelastic behavior can be effectively represented by a spring-dashpot system. Maxwell and Kelvin models are the two fundamental systems, representing a combination of a series and a parallel of a spring and a dashpot, respectively.[33] Combining the two fundamental models, the standard solid model, shown in Fig.4.2, was utilized to simulate the viscoelastic behavior of the TMV superlattice. The advantage of the standard solid model is that both the instantaneous elastic response and the retarded elastic response can be reflected, which better describes the mechanical response of most viscoelastic bodies. In addition, the constitutive equations for the standard solid model become simpler.

It is customary to assume that the volumetric response to hydrostatic stress is elastic deformation and thus is uniquely determined by the spring in series.[69]Then the four linear operators for the standard solid model can be expressed as

$$P^d = 1 + p_1^d \frac{\partial}{\partial t},\ Q^d = q_0^d + q_1^d \frac{\partial}{\partial t},\ P^m = 1,\ Q^m = 3K_1 \tag{4.11}$$

where $p_1^d = \frac{\eta}{G_1 + G_2}$, $q_0^d = \frac{2G_1 G_2}{G_1 + G_2}$, $q_1^d = \frac{2G_1 \eta}{G_1 + G_2}$, $G_1 = \frac{E_1}{2(1+v_1)}$, $G_2 = \frac{E_2}{2(1+v_2)}$, $K_1 = \frac{E_1}{3(1-2v_1)}$

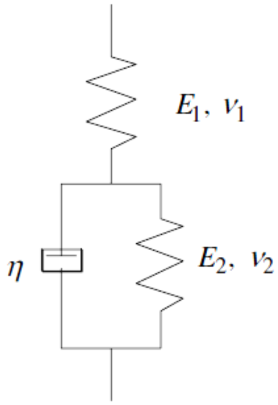

Figure 4.2. Schematic of the standard solid model.

Invoking the linear operators into Eq. (4.10), a functional differential equation is obtained

$$(\sum_{i=0}^{2} A_i \frac{\partial^i}{\partial t^i})[F(t) + 2\pi\omega R] = (4\sqrt{R}/3)(\sum_{i=0}^{2} B_i \frac{\partial^i}{\partial t^i})\delta^{3/2}(t) \tag{4.12}$$

where $A_0 = 2q_0 + 3K_1$, $A_1 = p_1(3K_1 + 2q_0) + (3p_1K_1 + 2q_1)$, $A_2 = p_1(3p_1K_1 + 2q_1)$,

$B_0 = q_0(1 + 6K_1)$, $B_1 = q_0(p_1 + 6K_1p_1) + q_1(6K_1 + 1)$, $B_2 = q_1(p_1 + 6K_1p_1)$

The functional equation obtained now extends the elastic solution of nanoindentation to viscoelastic system. Equation (4.12) relates the indentation load P with the relative approach δ. If the function of δ with respect to time, *t*, is known, the function of *P(t)* can be obtained by solving the differential equation above.

4.2. The transient viscoelastic measurement of TMV superlattice

4.2.1. Experiment

The TMV superlattice solution was obtained from the mixture of the TMV and $BaCl_2$ solution (molar ratio of Ba^{2+}: TMV = 9.2×10^4: 1), and further diluted with deionized water (volume ratio 1:1). The detailed TMV superlattice synthesis procedure can be found elsewhere [89]. A 10 μL drop of the diluted solution on a Si wafer was dispersed at 800 rpm for 10 s to form a mono-layer. The sample was dried for 30 min under ambient conditions (40% R.H., 21 ℃) for AFM (Veeco 3100) observation and mechanical testing.

To investigate the viscoelastic property of the TMV/Ba^{2+} superlattice, nanoindentation was performed using the AFM nanoindentation mode (AFM probe type: Tap150-G, Nanoandmore). The geometry of the AFM silicon probe was precisely measured using FESEM, with a length of 125 μm, width of 25 μm, and thickness of 2.1 μm. The tip radius is 12 nm. For a typical indentation test, the tip was pressed into the sample surface for ~12 nm, a depth that was comparable to the tip radius. A series of indentations with a constant initial indentation force but varying duration time were performed to track the viscoelastic responses. A 10 min time interval of the two adjacent indentations was set for the indentation to fully recover prior to the next indentation.

4.2.2. Solution to AFM-based nanoindentation

It is known that as the AFM tip is pressed down, it will stop until a predefined force, a corresponding deflection of cantilever is reached. To measure the viscoelasticity, AFM is able to define the duration time of indentation. During each indentation, the vertical distance between the substrate and the end of the cantilever is fixed. Due to the viscoelastic behavior of the sample, the deflection of the cantilever, or the normal indentation force, gradually decreases, the deformation, or the indentation depth, however, increases. A schematic of the stress relaxation is shown in Fig.4.4, where the force probed by the deflection of the cantilever decrease from ~100 nN to ~ 40 nN.

The modified standard solid model is shown to simulate the AFM-based nanoindentation on a viscoelastic material. Rather than establish a spring-dashpot model for the TMV superlattice only, the cantilever as a spring is also combined in the model. Hence, as the vertical distance between the substrate and the end of the cantilever does not change for each indentation, stress relaxation can be described by this modified standard solid model. During this process, the force on the system decreases while the deformation of sample increases to compensate the decreased deflection of the cantilever. In Fig.4.4, the change of the cantilever's deflection (Δ*d*) is equal to the sample's deformation (δ) during indentation. Hence, the distance between the end of cantilever and the substrate where the sample lies keeps constant.

To obtain the mathematical solution of the viscoelastic functional equation for the case of stress relaxation, assume *P(0),* $P^{'}(0)$and $P^{''}(0)$are all zeros at *t=0*. The indentation depth δ can be written as

$$\delta(t) = \delta_0 H(t) \qquad (4.13)$$

where *H(t)* is the Heaviside unit step function and δ_0 is the relative approach between the substrate and the end of the cantilever.

Thus Eq. (10) can be rewritten as

$$\left(\sum_{i=0}^{2} A_i \frac{\partial^i}{\partial t^i} \right)(F(t) + 2\pi\omega R) = (4\sqrt{R}/3)\delta_0^{3/2}\left(\sum_{i=0}^{2} B_i \frac{\partial^i}{\partial t^i} \right)H(t) \qquad (4.14)$$

Laplace transform was used to get an analytical solution for the loading history *F*(t).Applying Laplace transform on Eq. (4.14), we have

$$(A_0 + A_1 s + A_2 s^2)(\hat{F}(s) + \frac{2\pi\omega R}{s}) = (4\sqrt{R}/3)\delta_0^{3/2}(B_0 + B_1 s + B_2 s^2)\frac{1}{s} \qquad (4.15)$$

where a function with ^on its top means Laplace transformed function in *s* domain.

By dividing $(A_0 + A_1 s + A_2 s^2)$ on both sides of Eq. (4.15) and performing inverse Laplace transform, it yields

$$F(t)=\frac{4\sqrt{\delta_0^3 R}}{3}(A_r e^{-\alpha t}+B_r e^{-\beta t}+C_r)-2\pi\omega R \tag{4.16}$$

where $A_r=\frac{G_1^2}{G_1+G_2}$, $B_r=\frac{27G_1^2K_1^2}{(3K_1+4G_1)(3K_1G_1+3K_1G_2+4G_1G_2)}$,

$C_r=\frac{4G_1G_2}{G_1+G_2}(1-\frac{3G_1G_2}{3K_1G_1+3K_1G_2+4G_1G_2})$, $\alpha=\frac{G_1+G_2}{\eta}$, $\beta=\frac{G_2}{\eta}+\frac{3K_1G_1}{\eta(3K_1+4G_1)}$

This equation is referred to be the viscoelastic equation of AFM-based indentation.

The experimental data shown in Fig.4.3, exhibits the variation of force as a function of indentation time. The initial indentation force at t=0 was measured to be 104.21nN, then the force started to drop over time and remained steady at 38 nN after ~5000 ms. The descending process of force curve in Fig.4.3 fits qualitatively well with the exponential function which is derived in Eq. (4.16). The elastic modulus E_1, E_2 and viscosity η, corresponding to the parameters of mechanical properties in Fig.4.1, can then be determined by fitting Eq. (4.16) with the experimental data.

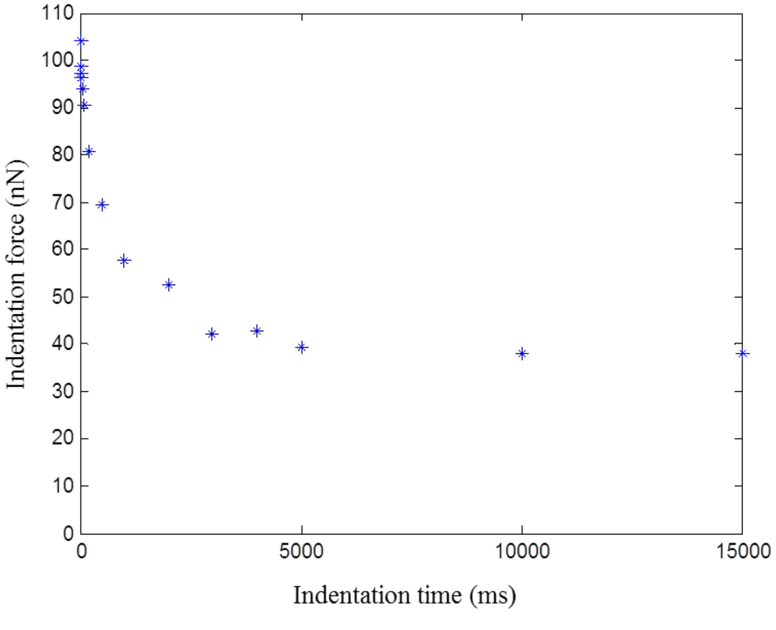

Figure 4.3. Variation of indentation force with respect to different indentation duration.

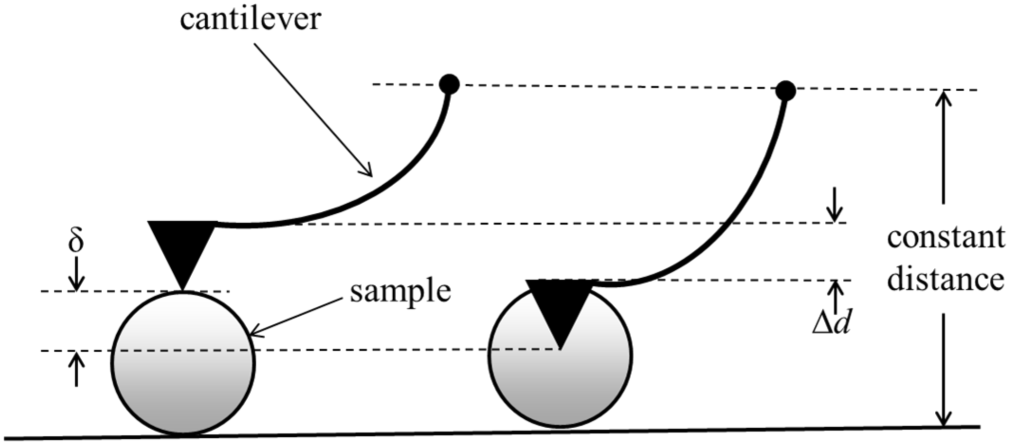

Figure 4.4. The variation of cantilever's deflection *(*Δd) and the sample's deformation (δ) during indentation.

From the initiation of contact to the maximum indentation depth, the relative approach between the substrate and the end of the cantilever, δ_0, is obtained from indentation data. In our case, δ_0=78.457 nm. The pull-off force, $2\pi\omega R$, calculated by averaging the pull-off forces of multiple indentations on the TMV superlattice, is determined to be ~16 nN. By comparison with the curvature of AFM tip, the surface of the sample can be treated as a flat plane. Hence, the nominal radius $R=R_{tip}$=12nm.

When *t=0*, Eq. (4.16) becomes

$$F(0)=\frac{16\sqrt{\delta_0^3 R}}{3}\frac{G_1(3K_1+G_1)}{3K_1+4G_1}-2\pi\omega R \tag{4.17}$$

With *F(0), R,* δ_0, $2\pi\omega R$, and the relationship that $G_1=E_1/2(1+v_1)$ and $K_1=E_1/3(1-2v_1)$ into the equation above, it gives

$$\frac{E_1}{1-v_1^2}=0.0375 \tag{4.18}$$

The method proposed in reference [56] can be adopted to determine the Poisson's ratio v_1. For simplicity, the Poisson's ratio is taken to be 0.38, a commonly used value for biological materials. Therefore $E_1$is determined to be 0.0320*GPa*.

When $t = \infty$, Eq. (4.16) becomes

$$F(\infty) = \frac{4\sqrt{\delta_0^3 R}}{3} C_r - 2\pi\omega R \tag{4.19}$$

The obtained equation contains only one unknown parameter, E_2, given v_2=0.38.Thus$E_2$is determined to be ~0.0213*GPa*.

Plugging the experimental data except at t=0 or t=∞ in Fig.4.3into Eq. (4.16), the value of viscosity can be determined. The viscoelastic equations were derived based on the assumption that the elastic modulus and viscosity are constants. It is found that when $\eta = 12.4\,\text{GPa}\cdot\text{ms}$, the coefficient of determination R^2 of the viscoelastic equation and the experimental data is maximum, which is ~0.9639.

Since the stress relaxation process is achieved by a combination of the cantilever and the sample, the viscoelasticity of the sample can be obtained by subtracting the component of cantilever from the results. The cantilever, acting as a spring, is in series with the sample, which is represented by a standard solid model. The schematic of the series organization is shown in Fig.4.5.

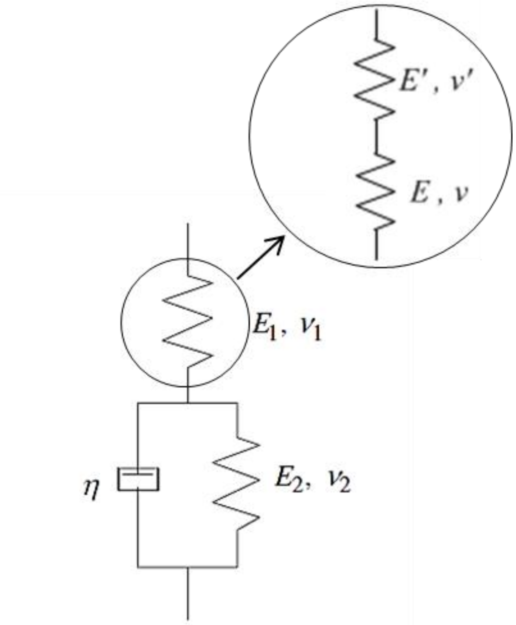

Figure 4.5. Spring-dashpot schematic of cantilever in series with sample.

At the initial of indentation, the spring with elastic modulus of E_1takes all the deformation, due to the instantaneous step load that the dashpot cannot take, resulting in no change of the spring with E_2. Therefore the viscous behavior is not present at the beginning and the whole indentation system can be treated as a pure elastic body. Hence, the elastic modulus of *E* can be acquired from the experimental data of zero duration indentation. Applying the DMT model in Eq. (4.7) to the contact between the tip and the sample, and considering the force-displacement relationship of the cantilever,

$$F = k\delta_{cantilever} \tag{4.20}$$

where *k* is the spring constant of the cantilever, which is 5 N/nm; $\delta_{cantilever}$ is deflection of the cantilever of AFM probe. The elastic equation of AFM- based indentation

$$\delta = \frac{F}{k} + \left(\frac{F + 2\pi\omega R}{E^{*}\sqrt{R}} \right)^{2/3} \tag{4.21}$$

where δ is recorded directly as the z-piezo displacement by AFM.

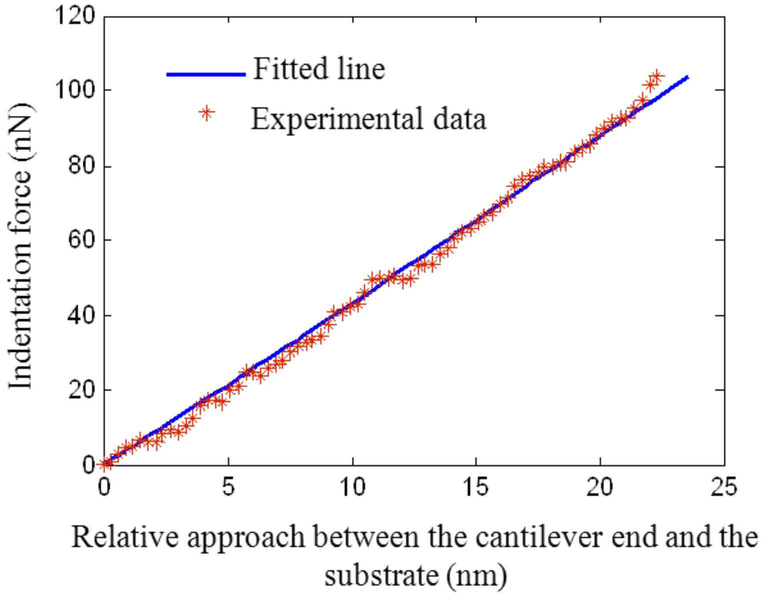

Figure 4.6. DMT-model-based indentation equation fitted with experimental data.

The elastic modulus of *E* can be calculated by fitting the DMT-model-based indentation equation with experimental data. For simplicity, some modification was done to the indentation equation and the experimental data, whose details can be found in reference [87]. The fitted elastic modulus of *E* is ~3 GPa with an coefficient of determination of 0.9948.

4.3. Results and discussion

Based on the solution obtained in the section above, the viscoelastic equation of AFM-based indentation for TMV superlattice can be put as

$$P(t) = 3.2098(0.0070e^{-\frac{0.0193t}{12.4}} + 0.0136e^{-\frac{0.0163t}{12.4}} + 0.0168) - 16 \qquad (4.22)$$

The equation was visually shown in Fig.4.7. in company with the experimental data.

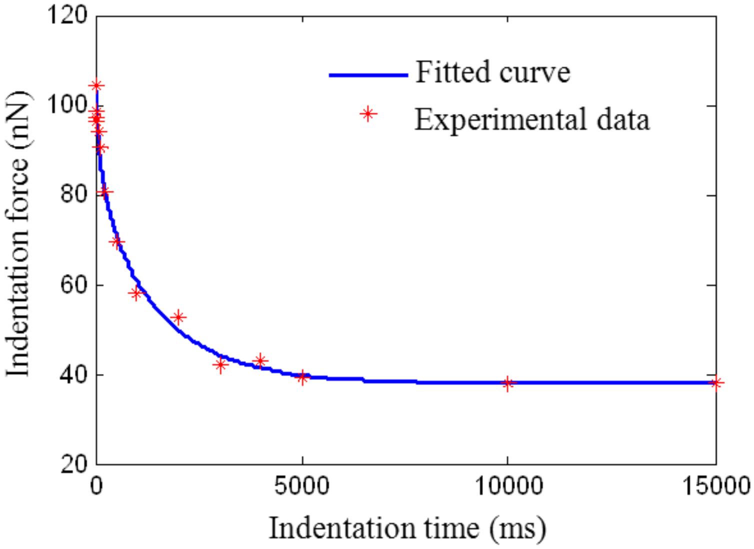

Figure 4.7. Indentation experimental data v.s. fitted indentation equations.

Specifically for the TMV superlattice whose viscoelastic stress-strain behavior is simulated by a standard solid model, the governing equation becomes

$$\dot{\sigma}+\frac{E_2}{\eta}\sigma=\frac{EE_2}{\eta}\varepsilon+(E+E_2)\dot{\varepsilon} \tag{4.23}$$

where E=3 GPa, E_2=0.0213 GPa, and $\eta = 12.4\,\text{GPa}\cdot\text{ms}$.

In the standard solid model, the spring with E responds to the indentation loading instantaneously. The initial experimental data point is completely determined by the instantaneous elastic modulus. At the beginning, the indentation force undertaken by the whole system is the largest and is equally taken by E and η. However, E_2 undertook no load initially due to the constraint of the paralleled dashpot. When the indentation was held for 5000 ms, the indentation force sensed by the probe tends to a constant, which is ~38 nN in this case. It means no displacement took place on the whole indentation system and thus the dashpot experienced no load. Then all the force was distributed on the two springs which were in series with each other. In contrast to E, $E_2$is much smaller and therefore the indentation force reduced by a large extent, from ~104 nN to ~38 nN. It can be calculated that the tip went down another 13.2 nm from the beginning of indentation.

4.4. Summary

This work introduced a novel method to perform the transient viscoelastic experiment on micro/nano-scale materials by using an AFM. By contrary to previous AFM-based dynamic methods for viscoelasticity measurement, the experiment proposed here is able to extract the viscosity and elasticity of the sample, respectively, instead of storage and loss moduli which are frequency-dependent properties. Accordingly, the results obtained from this experiment are applicable to a more general situation. Furthermore, the adhesion between the AFM tip and the sample surface is also taken account in this method and thus more accurate results can be achieved. Besides, the experiment is set up based on a basic AFM, without the need for sinusoidal displacement generating unit and thus is more convenient and cheaper to operate. The experiment was proposed based on a model of viscoelastic contact mechanics which evolved from elastic contact mechanics model. The derivation followed the approach of functional equation that has been justified to be an effective method to extend the elastic solution to viscoelastic solution. The elastic moduli and viscosity of superlattice formed by TMV was measured to be E=3 GPa, E_2=0.0213GPa, and $\eta = 12.4 GPa \cdot ms$, corresponding to the parameters denoted in the standard solid model in Fig. 4.5. It means the TMV superlattice is quite rigid at the initial contact and tends to experience a large deformation under a constant pressure.

CHAPTER 5. CONCLUSIONS AND FUTURE WORK

In this thesis, the elastic modulus, surface energy density and viscoelasticity of TMV superlattice were investigated. Particularly, some novel AFM-based techniques were developed to characterize the mechanical properties of micro/nano-biomaterials. By comparison with the previous methods for nanomechanical characterization, the methods proposed in this work are able to provide better results. The main contributions of this thesis are summarized into the following points.

1) Extended JKR model was employed to perform nanoindentation analysis and determine the elastic modulus of TMV superlattice via a newly proposed numerical process. The extended JKR model is more accurate than Hertz model to extract the elastic modulus. Even though the extended JKR model is much more complicated than Hertz model due to the uncertainty of the contact point, the newly proposed numerical method works effectively to fit the experimental data with the extended JKR model. The surface energy density, which is an important property to determine the interaction of biomaterials, is also able to be determined. The TMV superlattice has been found to be more rigid than individual TMVs. This results agree well with our estimation that superlattice is rigid than its constituents.

2) Transient viscoelastic nanoindentation experiment was for the first time proposed. By contrary to previous dynamic AFM-based viscoelastic experiments, the method proposed in this thesis is easier and economic to operate. More importantly, the viscoelasticity is quantitatively characterized by viscosity and elasticity instead of storage and loss moduli in this newly developed method. It makes the experiment apply to a wider range of materials. The numerical procedures to determine the viscosity and elasticity are based on a newly developed viscoelastic contact models. This model took the adhesion into consideration and thus provided more precise

results. The method has the potential to quantitatively characterize the nonlinear viscoelasticity of nanomaterial.

Besides of the additions to the nanomechanical characterization, some remaining work is to be addressed herein. They can strengthen the AFM as an effective tool for nanomechanical characterization.

1) The methods to determine the elastic modulus and viscoelasticity were essentially founded upon some contact mechanics models. All these models consider the most idealized situation. For example, the objects in contact are homogeneous and isotropic with perfect geometrical profile, such as plane or sphere. The reality, however, deviates from the ideal situation assumed by those models. Particularly, the anisotropy of samples should be accounted. By far, the only two publications of nanoindentation on anisotropic materials were from Dr. Vlassak at Harvard. But more knowledge on this subject needs to be gained so that we can obtain the anisotropic elasticity of nanomaterial safely and convincingly.

2) The finite element method should be an efficient and effective numerical tool to study the nano adhesive contact for various conditions. In reality, the samples are usually heterogeneous materials. The profile of contact interfaces can be extremely complex and thus challenging to formulate. Finite element simulation is an ideal method to solve those complicated problems. However, there is no adhesive contact analysis package in current commercial FEA software. Secondary development on the FEA software is needed. Before that, the applicability of FEA for nanomechanical system should be studied. A more convincing method to achieve this study is comparison between the FEA simulation results and atomic simulation results.

3) Superlattice has been found to feature excellent optical and semiconducting properties. Future work should measure these physical properties of TMV superlattice, which makes it possible to use the TMV superlattice in a wider range than biomedicine.

REFERENCES

[1] Zaitlin, M., 1998, "The Discovery of the Causal Agent of the Tobacco Mosaic Disease " Discoveries in Plant Biology, S. D. K. a. S. F. Yang, ed., World Publishing Co., Ltd., HongKong, pp. 105-110.

[2] Lee, L. A., Nguyen, Q. L., Wu, L. Y., Horyath, G., Nelson, R. S., and Wang, Q., 2012, "Mutant Plant Viruses with Cell Binding Motifs Provide Differential Adhesion Strengths and Morphologies," Biomacromolecules, 13(2), pp. 422-431.

[3] Manchester, M., and Singh, P., 2006, "Virus-based nanoparticles (VNPs): Platform technologies for diagnostic imaging," Advanced Drug Delivery Reviews, 58(14), pp. 1505-1522.

[4] O'Neil, A., Reichhardt, C., Johnson, B., Prevelige, P. E., and Douglas, T., 2011, "Genetically Programmed In Vivo Packaging of Protein Cargo and Its Controlled Release from Bacteriophage P22," Angewandte Chemie-International Edition, 50(32), pp. 7425-7428.

[5] Mao, C. B., Solis, D. J., Reiss, B. D., Kottmann, S. T., Sweeney, R. Y., Hayhurst, A., Georgiou, G., Iverson, B., and Belcher, A. M., 2004, "Virus-based toolkit for the directed synthesis of magnetic and semiconducting nanowires," Science, 303(5655), pp. 213-217.

[6] Bruckman, M. A., Soto, C. M., McDowell, H., Liu, J. L., Ratna, B. R., Korpany, K. V., Zahr, O. K., and Blum, A. S., 2011, "Role of Hexahistidine in Directed Nanoassemblies of Tobacco Mosaic Virus Coat Protein," Acs Nano, 5(3), pp. 1606-1616.

[7] Nam, K. T., Kim, D. W., Yoo, P. J., Chiang, C. Y., Meethong, N., Hammond, P. T., Chiang, Y. M., and Belcher, A. M., 2006, "Virus-enabled synthesis and assembly of nanowires for lithium ion battery electrodes," Science, 312(5775), pp. 885-888.

[8] Scofield, S. R., and Nelson, R. S., 2009, "Resources for Virus-Induced Gene Silencing in the Grasses," Plant Physiology, 149(1), pp. 152-157.

[9] Burch-Smith, T. M., Anderson, J. C., Martin, G. B., and Dinesh-Kumar, S. P., 2004, "Applications and advantages of virus-induced gene silencing for gene function studies in plants," Plant Journal, 39(5), pp. 734-746.

[10] Liu, L., Canizares, M. C., Monger, W., Perrin, Y., Tsakiris, E., Porta, C., Shariat, N., Nicholson, L., and Lomonossoff, G. P., 2005, "Cowpea mosaic virus-based systems for the production of antigens and antibodies in plants," Vaccine, 23(15), pp. 1788-1792.

[11] Rasmussen, N., 2003, "The life of a virus: Tobacco mosaic virus as an experimental model, 1930-1965," Bulletin of the History of Medicine, 77(1), pp. 221-223.

[12] Klug, A., 1999, "The tobacco mosaic virus particle: structure and assembly," Philosophical Transactions of the Royal Society of London Series B-Biological Sciences, 354(1383), pp. 531-535.

[13] Wang, X. N., Niu, Z. W., Li, S. Q., Wang, Q., and Li, X. D., 2008, "Nanomechanical characterization of polyaniline coated tobacco mosaic virus nanotubes," Journal of Biomedical Materials Research Part A, 87A(1), pp. 8-14.

[14] Pfleger, F. L., and Zeyen, R. Z., 2008, "Tomato-Tobacco Mosaic Virus Disease."

[15] Ashkin, A., and Dziedzic, J. M., 1987, "Opticaltrappingand manipulationofvirusesandbacteria," Science, 235(4795), pp. 1517-1520.

[16] Splettstoesser, T., 2012, "Tobacco mosaic virus."

[17] Namba, K., and Stubbs, G., 1986, "Structureof tobacco mosaic-virusat 3.6-A resolution - implication for assembly," Science, 231(4744), pp. 1401-1406.

[18] Petrie, T. A., Raynor, J. E., Dumbauld, D. W., Lee, T. T., Jagtap, S., Templeman, K. L., Collard, D. M., and Garcia, A. J., 2010, "Multivalent Integrin-Specific Ligands Enhance Tissue Healing and Biomaterial Integration," Science Translational Medicine, 2(45).

[19] Wu, L. Y., Zang, J. F., Lee, L. A., Niu, Z. W., Horvatha, G. C., Braxtona, V., Wibowo, A. C., Bruckman, M. A., Ghoshroy, S., zur Loye, H. C., Li, X. D., and Wang, Q., 2011, "Electrospinning fabrication, structural and mechanical characterization of rod-like virus-based composite nanofibers," Journal of Materials Chemistry, 21(24), pp. 8550-8557.

[20] Tseng, R. J., Tsai, C. L., Ma, L. P., and Ouyang, J. Y., 2006, "Digital memory device based on tobacco mosaic virus conjugated with nanoparticles," Nature Nanotechnology, 1(1), pp. 72-77.

[21] Li, T., Winans, R. E., and Lee, B., 2011, "Superlattice of Rodlike Virus Particles Formed in Aqueous Solution through Like-Charge Attraction," Langmuir, 27(17), pp. 10929-10937.

[22] Koehler, J. S., 1970, "Attempt to Design a Strong Solid," Physical Review B, 2(2), pp. 547-551.

[23] Yashar, P., Barnett, S. A., Rechner, J., and Sproul, W. D., 1998, "Structure and mechanical properties of polycrystalline CrN/TiN superlattices," Journal of Vacuum Science & Technology A, 16(5), pp. 2913-2918.

[24] Xu, J. H., Li, G. Y., and Gu, M. Y., 2000, "The microstructure and mechanical properties of TaN/TiN and TaWN/TiN superlattice films," Thin Solid Films, 370(1-2), pp. 45-49.

[25] Travesset, A., "Self-Assembly Enters the Design Era," Science, 334(6053), pp. 183-184.

[26] Hultman, L., Engstrom, C., and Oden, M., 2000, "Mechanical and thermal stability of TiN/NbN superlattice thin films," Surface & Coatings Technology, 133, pp. 227-233.

[27] Wu, M. J., Wen, H. C., Wu, S. C., Yang, P. F., Lai, Y. S., Hsu, W. K., Wu, W. F., and Chou, C. P., 2011, "Nanomechanical characteristics of annealed Si/SiGe superlattices," Applied Surface Science, 257(21), pp. 8887-8893.

[28] Jaskolski, W., and Pelc, M., 2008, "Carbon nanotube superlattices in a magnetic field," International Journal of Quantum Chemistry, 108(12), pp. 2261-2266.

[29] Lyding, J. W., 2009, "CARBON NANOTUBES A simple approach to superlattices," Nature Nanotechnology, 4(9), pp. 545-546.

[30] Nikoobakht, B., Wang, Z. L., and El-Sayed, M. A., 2000, "Self-assembly of gold nanorods," Journal of Physical Chemistry B, 104(36), pp. 8635-8640.

[31] Sreeprasad, T. S., Samal, A. K., and Pradeep, T., 2008, "One-, two-, and three-dimensional superstructures of gold nanorods induced by dimercaptosuccinic acid," Langmuir, 24(9), pp. 4589-4599.

[32] Xie, Y., Guo, S. M., Ji, Y. L., Guo, C. F., Liu, X. F., Chen, Z. Y., Wu, X. C., and Liu, Q., 2011, "Self-Assembly of Gold Nanorods into Symmetric Superlattices Directed by OH-Terminated Hexa(ethylene glycol) Alkanethiol," Langmuir, 27(18), pp. 11394-11400.

[33] Ethier, C. R., and Simmons, C. A., 2007, Introductory Biomechanics, Cambridge University Press, New York, US.

[34] Falvo, M. R., Washburn, S., Superfine, R., Finch, M., Brooks, F. P., Chi, V., and Taylor, R. M., 1997, "Manipulation of individual viruses: Friction and mechanical properties," Biophys. J., 72(3), pp. 1396-1403.

[35] Schmatulla, A., Maghelli, N., and Marti, O., 2007, "Micromechanical properties of tobacco mosaic viruses," Journal of Microscopy-Oxford, 225(3), pp. 264-268.

[36] Zhao, Y., Ge, Z. B., and Fang, J. Y., 2008, "Elastic modulus of viral nanotubes," Physical Review E, 78(3).

[37] Lakes, R. S., 2004, "Viscoelastic measurement techniques," Review of Scientific Instruments, 75(4), pp. 797-810.

[38] Mahaffy, R. E., Shih, C. K., MacKintosh, F. C., and Kas, J., 2000, "Scanning probe-based frequency-dependent microrheology of polymer gels and biological cells," Physical Review Letters, 85(4), pp. 880-883.

[39] Yuya, P. A., Hurley, D. C., and Turner, J. A., 2008, "Contact-resonance atomic force microscopy for viscoelasticity," Journal of Applied Physics, 104(7).

[40] Yablon, D. G., Gannepalli, A., Proksch, R., Killgore, J., Hurley, D. C., Grabowski, J., and Tsou, A. H., 2012, "Quantitative Viscoelastic Mapping of Polyolefin Blends with Contact Resonance Atomic Force Microscopy," Macromolecules, 45(10), pp. 4363-4370.

[41] Wahl, K. J., Stepnowski, S. V., and Unertl, W. N., 1998, "Viscoelastic effects in nanometer-scale contacts under shear," Tribology Letters, 5(1), pp. 103-107.

[42] MacKintosh, F. C., and Schmidt, C. F., 1999, "Microrheology," Current Opinion in Colloid & Interface Science, 4(4), pp. 300-307.

[43] Cheng, L., Xia, X., Yu, W., Scriven, L. E., and Gerberich, W. W., 2000, "Flat-punch indentation of viscoelastic material," Journal of Polymer Science Part B-Polymer Physics, 38(1), pp. 10-22.

[44] Cheng, L., Xia, X., Scriven, L. E., and Gerberich, W. W., 2005, "Spherical-tip indentation of viscoelastic material," Mechanics of Materials, 37(1), pp. 213-226.

[45] Jager, A., Lackner, R., and Eberhardsteiner, J., 2007, "Identification of viscoelastic properties by means of nanoindentation taking the real tip geometry into account," Meccanica, 42(3), pp. 293-306.

[46] Radok, J. R. M., 1957, "Visco-elastic stress analysis," Quart. Appl. Math., 15(2), pp. 198-202.

[47] Binnig, G. K., 1987, "Atomic-force microscope," Physica Scripta, T19A, pp. 53-54.

[48] Rugar, D., and Hansma, P., 1990, "Atomic force microscopy," Physics Today, 43(10), pp. 23-30.

[49] Shu Peng, J. O. K., Chengyu Wei, K. Cho*, 2001, "Carbon Nanotube Chemical and Mechanical Sensors," the 3rd International Workshop on Structural Health MonitoringStanford University, p. 8.

[50] Wang, H., Wang, X., Li, T., and Lee, B., 2013, "Nanomechanical characterization of rod-like superlattice assembled from tobacco mosaic viruses," Journal of Applied Physics, 113(2).

[51] Cappella, B., and Dietler, G., 1999, "Force-distance curves by atomic force microscopy," Surface Science Reports, 34(1-3), pp. 1-+.

[52] Lin, D. C., Dimitriadis, E. K., and Horkay, F., 2007, "Robust strategies for automated AFM force curve analysis - I. Non-adhesive indentation of soft, inhomogeneous materials," Journal of Biomechanical Engineering-Transactions of the Asme, 129(3), pp. 430-440.

[53] Oliver, W. C., and Pharr, G. M., 1992, "An improved technique fordetermining hardness and elastic-modulususing load and displacementsensing indentationexperiments," Journal of Materials Research, 7(6), pp. 1564-1583.

[54] "http://www.nanoandmore.com/USA/afm_probes.php."

[55] Bhushan, B., Mokashi, P. S., and Ma, T., 2003, "A technique to measure Poisson's ratio of ultrathin polymeric films using atomic force microscopy," Review of Scientific Instruments, 74(2), pp. 1043-1047.

[56] Hurley, D. C., and Turner, J. A., 2007, "Measurement of Poisson's ratio with contact-resonance atomic force microscopy," Journal of Applied Physics, 102(3).

[57] Bhushan, B., 2001, "Nano- to microscale wear and mechanical characterization using scanning probe microscopy," Wear, 251, pp. 1105-1123.

[58] Cheng, Y. T., and Cheng, C. M., 2000, "What is indentation hardness?," Surface & Coatings Technology, 133, pp. 417-424.

[59] Urena, A., Rams, J., Escalera, M. D., and Sanchez, M., 2005, "Characterization of interfacial mechanical properties in carbon fiber/aluminium matrix composites by the nanoindentation technique," Composites Science and Technology, 65(13), pp. 2025-2038.

[60] Maugis, D., 1995, "Extensionofthe Johnson-Kendall-Robertstheory of theelastic contact of spheresto large contact radii," Langmuir, 11(2), pp. 679-682.

[61] Johnson, K. L., 1992, Contact mechanics, Cambridge university press, Cambridge, UK.

[62] Johnson, K. L., Kendall, K., and Roberts, A. D., 1971, "Surface energy andcontact ofelastic solids," Proceedings of the Royal Society of London Series a-Mathematical and Physical Sciences, 324(1558), pp. 301-&.

[63] Lin, D. C., Dmitriadis, E. K., and Horkay, F., 2007, "Robust strategies for automated AFM force curve Analysis-II: Adhesion-influenced indentation of soft, elastic materials," Journal of Biomechanical Engineering-Transactions of the Asme, 129(6), pp. 904-912.

[64] Notbohm, J., Poon, B., and Ravichandran, G., 2012, "Analysis of nanoindentation of soft materials with an atomic force microscope," Journal of Materials Research, 27(1), pp. 229-237.

[65] Derjaguin, B. V., Muller, V. M., and Toporov, Y. P., 1975, "Effect of contactdeformationsof particles," Journal of Colloid and Interface Science, 53(2), pp. 314-326.

[66] Bradley, R. S., 1932, "The cohesive force between solid surfaces and the surface energy of solids," Philosophical Magazine, 13(86), pp. 853-862.

[67] Maugis, D., 1992, "Adhesion of spheres - The JKR-DMT transition usinga dugdalemodel," Journal of Colloid and Interface Science, 150(1), pp. 243-269.

[68] Johnson, K. L., and Greenwood, J. A., 1997, "An adhesion map for the contact of elastic spheres," Journal of Colloid and Interface Science, 192(2), pp. 326-333.

[69] Malvern, L. E., 1969, Introduction to the Mechanics of a Continuous Medium, Prentice-Hall, Inc., Englewood Cliffs, New Jersey.

[70] Shaw, M. T., and MacKnight, W. J., 2005, Introduction to Polymer Viscoelasticity, John Wiley & Sons, Inc., Hoboken, New Jersey.

[71] Christensen, R. M., 2003, Theory of Viscoelasticity, Dover Publications, Inc., Mineola, New York.

[72] Tseytlin, Y. M., 2008, "Atomic force microscope cantilever spring constant evaluation for higher mode oscillations: A-kinetostatic method," Review of Scientific Instruments, 79(2).

[73] Hutter, J. L., and Bechhoefer, J., 1993, "Calibration of atomic-force microscope tips," Rev. Sci. Instrum., 64(7), pp. 1868-1873.

[74] Sader, J. E., Larson, I., Mulvaney, P., and White, L. R., 1995, "Method for the calibrationof atomic-force microscopecantilevers," Review of Scientific Instruments, 66(7), pp. 3789-3798.

[75] Torii, A., Sasaki, M., Hane, K., and Okuma, S., 1996, "A method for determining the spring constant of cantilevers for atomic force microscopy," Meas. Sci. Technol., 7(2), pp. 179-184.

[76] Golovko, D. S., Haschke, T., Wiechert, W., and Bonaccurso, E., 2007, "Nondestructive and noncontact method for determining the spring constant of rectangular cantilevers," Review of Scientific Instruments, 78(4).

[77] Carrillo, F., Gupta, S., Balooch, M., Marshall, S. J., Marshall, G. W., Pruitt, L., and Puttlitz, C. M., 2005, "Nanoindentation of polydimethylsiloxane elastomers: Effect of crosslinking, work of adhesion, and fluid environment on elastic modulus," Journal of Materials Research, 20(10), pp. 2820-2830.

[78] Gupta, S., Carrillo, F., Li, C., Pruitt, L., and Puttlitz, C., 2007, "Adhesive forces significantly affect elastic modulus determination of soft polymeric materials in nanoindentation," Materials Letters, 61(2), pp. 448-451.

[79] Johnson, K. L., Kendall, K., and Roberts, A. D., 1971, "Surface energy and contact of elastic solids," Proceedings of the Royal Society of London Series a-Mathematical and Physical Sciences, 324(1558), pp. 301-313.

[80] Tabor, D., 1977, "Surface forcesand surface interactions," Journal of Colloid and Interface Science, 58(1), pp. 2-13.

[81] Ebenstein, D. M., 2011, "Nano-JKR force curve method overcomes challenges of surface detection and adhesion for nanoindentation of a compliant polymer in air and water," Journal of Materials Research, 26(8), pp. 1026-1035.

[82] Liao, Q. Z., Huang, J. Y., Zhu, T., Xiong, C. Y., and Fang, J., 2010, "A hybrid model to determine mechanical properties of soft polymers by nanoindentation," Mechanics of Materials, 42(12), pp. 1043-1047.

[83] Crick, S. L., and Yin, F. C. P., 2007, "Assessing micromechanical properties of cells with atomic force microscopy: importance of the contact point," Biomechanics and Modeling in Mechanobiology, 6(3).

[84] Cao, Y. F., Yang, D. H., and Soboyejoy, W., 2005, "Nanoindentation method for determining the initial contact and adhesion characteristics of soft polydimethylsiloxane," Journal of Materials Research, 20(8).

[85] Halpin, J. C., and Kardos, J. L., 1976, "Halpipn-Tsaiequations - Review," Polymer Engineering and Science, 16(5), pp. 344-352.

[86] Lee, E. H., 1955, "Stressanalysisinvisco-elastic bodies," Quart. Appl. Math., 13(2), pp. 183-190.

[87] Wang, H. R., Wang, X. N., Li, T., and Lee, B., 2013, "Nanomechanical characterization of rod-like superlattice assembled from tobacco mosaic viruses," Journal of Applied Physics, 113(2).

[88] Sneddon, I. N., 1965, "The relation between load and penetration in the axisymmetric Boussinesq problem for a punch of arbitrary profile," Int. J. Engng Sci., 3(1), pp. 47-57.

[89] Li, T., Winans, R. E., and Lee, B., "Superlattice of Rodlike Virus Particles Formed in Aqueous Solution through Like-Charge Attraction," Langmuir, 27(17), pp. 10929-10937.

[90] Ren, Z. Y., and Zheng, Q. S., 2002, "A quantitative study of minimum sizes of representative volume elements of cubic polycrystals - numerical experiments," Journal of the Mechanics and Physics of Solids, 50(4), pp. 881-893.

[91] Zheng, Q. S., and Hwang, K. C., 1996, "Reduced dependence of defect compliance on matrix and inclusion elastic properties in two-dimensional elasticity," Proceedings of the Royal Society of London Series a-Mathematical Physical and Engineering Sciences, 452(1954), pp. 2493-2507.

[92] Sauer, R. A., and Li, S. F., 2007, "A contact mechanics model for quasi-continua," International Journal for Numerical Methods in Engineering, 71(8), pp. 931-962.

[93] Sauer, R. A., and Wriggers, P., 2009, "Formulation and analysis of a three-dimensional finite element implementation for adhesive contact at the nanoscale," Computer Methods in Applied Mechanics and Engineering, 198(49-52), pp. 3871-3883.

APPENDIX. FINITE ELEMENT FORMULATION OF NANOINDENTATION

The appendix here is to formulate the FE model of adhesive contact. This work will be divided into three major parts. 1). the minimum sizes for FE method. Since the FE method was built upon the theories of continuum mechanics, the applicability of this method for micro/nano system is strongly challenged. As the first part, the minimum sizes where the assumption of continuum medium still holds will be quantitatively characterized. 2). The FE simulation of general contact problem. In this part, some basic philosophies behind the contact analysis in FE will be covered. 3). The FE formulation of adhesive forces into the contact system.

A.1. The applicability of finite element method for nanoscale problem

For polycrystals, the constraints for the sizes of FE method are mainly from the anisotropy and the different orientation of crystals in it. When the polycrystals under investigation were scaled down to the sizes comparable to that of its grains, the mechanical properties, e.g., the Young's modulus and shear modulus observed in that scale will be different from those observed in bulk scale. On the other hand, the monocrystal can be scaled down to an infinitesimal size which is effective for FE method. This can also be derived as a special case in polycrystals where the anisotropic degree is 0. It has been proved in the tensor representative theory by Nye. *et al*. that the linear thermal conductivity is always isotropic for any cubic crystals and thus the size for thermal problem in FE method can be as small as possible; the linear elasticity is not always isotropic for all cubic crystals so there is a minimum size for elastic solid problem in FE simulation. It is noted that the minimum size of effective volume for different mechanical properties are also different.

Before calculating the minimum sizes for effective volume, we'll first define the concept of effective volume size. From the perspective in macro-scale, a bulk of material is homogeneous in its mechanical properties due to the randomly distributed anisotropic grains. When a bulk of polycrystal is subject to uniformly distributed stress, $\boldsymbol{\sigma}$, a uniform strain will be resulted which is denoted by the second-order tensor, $\boldsymbol{\varepsilon}$. The stress and strain mentioned above is a behavior demonstrated by the whole bulk of material. They are what we use usually based on the assumption of continuum medium. From the mechanics of materials, the stress tensor and strain tensor are related by a fourth-order tensor, ***C***, the stiffness tensor, or ***S***, the compliance tensor. However, when we look at a small sub-volume in the bulk material with size *d*, we can obtain a new set of stress, strain and compliance tensor. To distinguish them from the previous ones, they are denoted by $\boldsymbol{\sigma}_\mathbf{d}, \boldsymbol{\varepsilon}_\mathbf{d}$ and $\boldsymbol{S_d}$, respectively. The compliance tensor is derived from Young's modulus and Poisson's ratio, and thus is a material-dependent parameter. When the size of the sub-volume is small enough, $\boldsymbol{S_d}$ will deviate from ***S*** due to the anisotropic of the grains**.** There exists a critical size, below which the deviation occurs. The critical size is the effective volume size we are going to calculate.

A schematic of different orientations of crystals and different sizes of sub-volume can be found in Fig.A.1. For a sub-volume of a specific size chosen, the stress-strain relationship follows Hooke's law,

$$\varepsilon_{\mathrm{ij}}^{d} = \frac{1}{E_d}[(1+v_d)\sigma_{ij}^{d} - v_d \sigma_{kk}^{d} \delta_{ij}] \qquad \text{(A.1)}$$

where δ_{ij} is the Kronecker delta.

For simplicity, we take the sub-volume to be in a plane stress state. Then Eq.A.1 gives rise to the following relationship to obtain the apparent Young's modulus and Poisson's ratio

$$E_d = \frac{\sigma_{11}^d \sigma_{11}^d - \sigma_{22}^d \sigma_{22}^d}{\sigma_{11}^d \varepsilon_{11}^d - \sigma_{22}^d \varepsilon_{22}^d}, \tag{A.2}$$

$$v_d = \frac{\sigma_{22}^d \varepsilon_{11}^d - \sigma_{11}^d \varepsilon_{22}^d}{\sigma_{11}^d \varepsilon_{11}^d - \sigma_{22}^d \varepsilon_{22}^d} \tag{A.3}$$

Then the apparent shear modulus and area modulus can be calculated by

$$G_d = \frac{E_d}{2(1+v_d)}, \kappa_d = \frac{E_d}{2(1-v_d)} \tag{A.4}$$

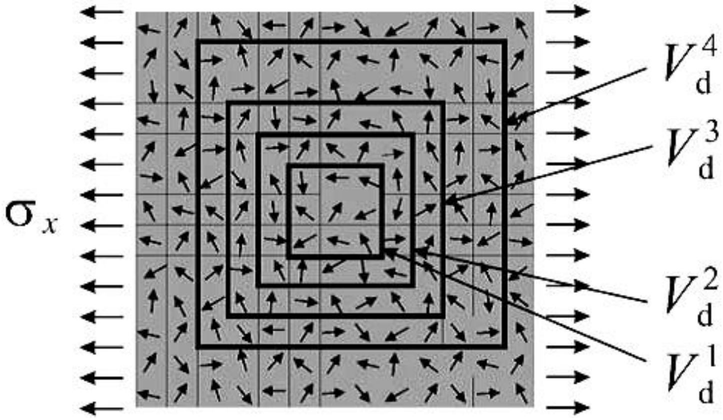

Figure A1. Different orientations of grains and different sizes of sub-volume.[90]

As the size of sub-volume increases, e.g., from V_d^1 to V_d^4 in Fig.A1, the shear modulus and area modulus tend to approach a constant. Such a tendency can be found in Fig.A.2.

The critical size to reach the contact modulus value is found to be relevant to the anisotropic degree. Then let's find the way to quantitatively characterize the degree of anisotropy. The compliance tensor of a sub-volume can be put into

$$\boldsymbol{S_d} = \frac{1}{E}[(1+v)\boldsymbol{I} - v\boldsymbol{1} \otimes \boldsymbol{1} + \boldsymbol{1} \otimes \boldsymbol{d_d} + \boldsymbol{d_d} \otimes \boldsymbol{1} + \boldsymbol{D}_d] \tag{A.5}$$

where $\boldsymbol{1}$ and $\boldsymbol{I}$ represent the identity tensors of second order and fourth order, respectively; $\boldsymbol{d_d}$ and $\boldsymbol{D_d}$ are sub-volume-dependent tensors and defined by the following equations

$$\boldsymbol{d_d} = a_2\boldsymbol{P_2} + b_2\boldsymbol{Q_2}, \boldsymbol{D_d} = a_4\boldsymbol{P_4} + b_4\boldsymbol{Q_4} \tag{A.6}$$

$$\boldsymbol{P_2} + \boldsymbol{Q_2}\mathrm{i} = (\boldsymbol{i_1} + \mathrm{i}\boldsymbol{i_2}) \otimes (\boldsymbol{i_1} + \mathrm{i}\boldsymbol{i_2}), \boldsymbol{P}_4 + \boldsymbol{Q}_4\mathrm{i} = (\boldsymbol{P_2} + \boldsymbol{Q_2}\mathrm{i}) \otimes (\boldsymbol{P_2} + \boldsymbol{Q_2}\mathrm{i}), \mathrm{i} = \sqrt{-1} \tag{A.7}$$

$$\frac{1}{E_c} = \frac{1}{2\pi}\int_0^{2\pi}\frac{1}{E_c(\theta)}d\theta, a_2 = \frac{E_c}{\pi}\int_0^{2\pi}\frac{\cos 2\theta}{E_c(\theta)}, b_2 = \frac{E_c}{\pi}\int_0^{2\pi}\frac{\sin 2\theta}{E_c(\theta)} \tag{A.8}$$

$$a_4 = \frac{E_c}{\pi}\int_0^{2\pi}\frac{\cos 4\theta}{E_c(\theta)}, b_4 = \frac{E_c}{\pi}\int_0^{2\pi}\frac{\sin 4\theta}{E_c(\theta)},$$

For more details of the derivation of the equations above as well as their physical interpretation, please refer to the reference [91]. The tensors $\boldsymbol{d_d}$ and $\boldsymbol{D_d}$ are related to the anisotropy of the sub-volume, which can be concluded from the equation above. When the sub-volume is isotropic, then the two tensors are zero tensors. Equation A5 evolves into the compliance tensor for isotropic material, which is a special case for anisotropy. Thus we have

$$\boldsymbol{S}_d^{iso} = \frac{1}{E}[(1+v)\boldsymbol{I} - v\boldsymbol{1}\otimes\boldsymbol{1}] \tag{A.9}$$

Combining Eq. A5 and Eq. A9, we obtain the equation for measuring the anisotropy degree as below,

$$\Delta(\boldsymbol{S}) = \frac{\left\|\boldsymbol{S_d} - \boldsymbol{S_d^{iso}}\right\|}{\left\|\boldsymbol{S_d}\right\|} \tag{A.10}$$

where $\|\boldsymbol{S}\| = \sqrt{S_{ijkl}S_{ijkl}}$.

A correlation between the critical sizes and the anisotropy degree can be found in Fig.A.3.

Then by numerical simulation of more than 574 different samples, their critical sizes for area modulus and shear modulus were obtained. The results indicate that the critical sizes for area modulus can be infinitesimal, while the critical sizes for shear modulus vary with anisotropy degree. A general linear correlation between the critical sizes and the anisotropy degree can thus be obtained according to the least square correlation method. With the variation of the error for shear modulus, the critical sizes will change a little accordingly. Then we can describe the relationship as $d_{RVE}^{G} = R(\delta)\Delta(S)$. Judged from the simulation results in Fig.A.3, the critical sizes for most materials are ~15 or fewer times than their critical sizes. Thus the continuum assumption mostly works well for nanomechanical problems. However, a case-by-case analysis is necessary. From Fig.A.3, we can also observe that the critical sizes for isotropic materials or materials with very small anisotropy degree tend to be 0.

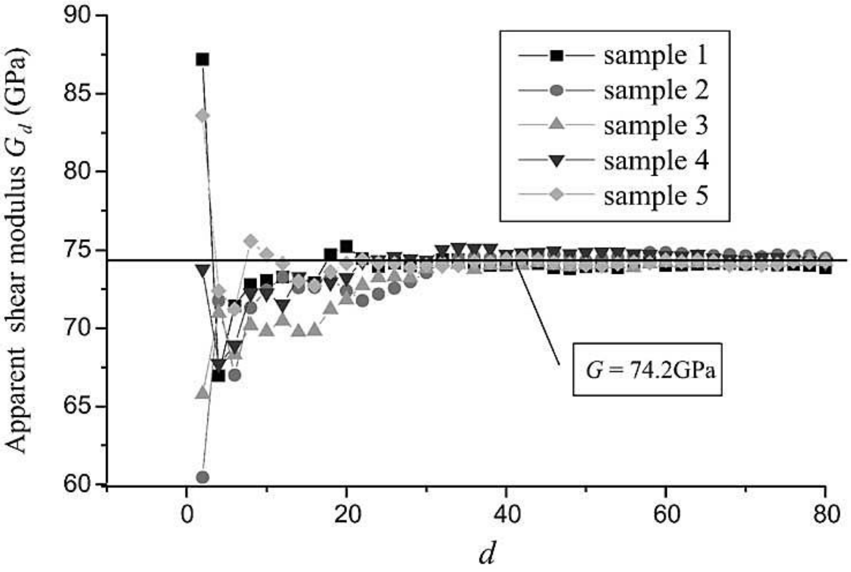

Figure A2. Apparent shear modulus varies with the size of sub-volume by numerical simulation.[90]

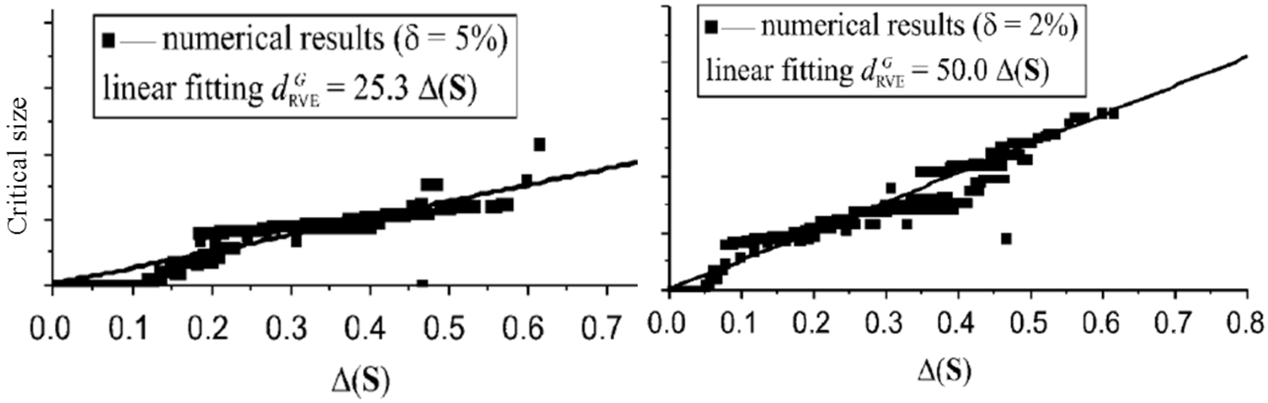

Figure A3. Critical size v.s. anisotropy degree by simulation of 574 cubic crystals.[90]

A.2. Finite element formulation of general contact system

To identify different surfaces in contact and assign different conditions, the in-contact surfaces are usually labeled with target and contact. There are several ways to identify the target and contact surfaces. 1) if one surface keeps static while the other one initiates the relative approach, the static surface is target and the moving one is contact; 2) The rigid surface is always defined to be target while the deformable one contact; 3) in other cases, the target and contact surfaces can be randomly assigned usually.

For convenience in the following statement, the quantities of target surface are labeled with a superscript, t, and the quantities of the contact surface with a superscript, c.

A.2.1. Contact point and gap

For three dimensional element, all three sides are mapped with the parameter *a* and *b* as x(*a*,*b*), y(*a*,*b*), and z(*a*,*b*). The normal vector of this element can then be calculated by

$$\boldsymbol{n} = \boldsymbol{v}_1 \times \boldsymbol{v}_2 \tag{A.11}$$

where $\boldsymbol{v_1} = (\frac{\partial x}{\partial a}, \frac{\partial y}{\partial a}, \frac{\partial z}{\partial a})^T, \boldsymbol{v}_2 = (\frac{\partial x}{\partial b}, \frac{\partial y}{\partial b}, \frac{\partial z}{\partial b})^T$

The potential contact point on the target surface corresponding to a point on the contact surface (x^c, y^c, z^c) can be obtained by means of least square method with the following condition

$$\min[(x^t - x^c)^2 + (y^t - y^c)^2 + (z^t - z^c)^2] \tag{A.12}$$

A.2.2. Finite element equations formulation through Lagrange multiplier weak form

Based on the equation that

Internal virtual work = body force work + surface force work – work by contact force

We can obtain the weak form of the contact problem

$$\iiint_V \delta\boldsymbol{\varepsilon}^T \boldsymbol{\sigma} dV = \iiint_V \delta\boldsymbol{u}^T \boldsymbol{b} dV + \iint_{A_q} \delta\boldsymbol{u}^T \boldsymbol{q} dA - \iint_{A_C} (\delta u_n^t - \delta u_n^c) F_n dA \tag{A.13}$$

where $\boldsymbol{\varepsilon}$ and $\boldsymbol{\sigma}$ are the strain and stress within an element, $\delta\boldsymbol{u}$ is the displacement increment, $\boldsymbol{b}$ and $\boldsymbol{q}$ are body force and surface force vectors, F_n is the normal forces between the contact surfaces, u_n^t and u_n^c are normal displacement of target and contactor surfaces.

To prevent the penetration between the two contact surfaces, the following constraint needs to be satisfied

$$\iint_{A_C} (u_n^t - u_n^c) \delta F_n dA \geq 0 \tag{A.14}$$

The final finite element model is

$$\begin{pmatrix} \boldsymbol{k} & \boldsymbol{k_c^T} \\ \boldsymbol{k_c} & \boldsymbol{0} \end{pmatrix} \begin{pmatrix} \boldsymbol{d} \\ \boldsymbol{F} \end{pmatrix} \begin{matrix} = \\ \leq \end{matrix} \begin{pmatrix} \boldsymbol{r_b} + \boldsymbol{r_q} \\ \boldsymbol{0} \end{pmatrix} \tag{A.15}$$

where $\boldsymbol{k} = \iiint\limits_{v} \boldsymbol{BCB}^T dV; \boldsymbol{k_c} = \iint\limits_{A_C} \boldsymbol{N_F n}^T \boldsymbol{N}^T dA; \boldsymbol{r_q} = \iint\limits_{A_q} \boldsymbol{Nq} dS; \boldsymbol{r_b} = \iiint\limits_{V} \boldsymbol{Nb} dV$

A.2.3. Finite element equations formulation through penalty formulation

The normal force at contact surfaces is expressed as

$$F_n = \begin{cases} 0 & \text{if no contact occurs} \\ \beta(u_n^t\text{-}u_n^c) & \text{if contact occurs} \end{cases}$$

where β is penalty parameter.

The final FE equations are obtained as

$$(\boldsymbol{k} + \boldsymbol{k}_p)\boldsymbol{d} = \boldsymbol{r} \tag{A.16}$$

where $k_p = \iint\limits_{A_c} \beta N n n^T N^T dA$

A.2.4. Comparison of Lagrange method and penalty method

To compare the simulation results through Lagrange and penalty methods, a simulation of contact between a sphere and a cylinder was performed in ANSYS. A schematic of the contact system was shown in Fig.A5. The sphere was assigned to be the target with rigid materials while the cylinder was assigned to be the contactor. The cylinder is a composite structure composed of isotropic matrix and tubular filler. Their elastic moduli were 1.0 GPa and 2.5 GPa , respectively, and their Poisson’s ratio was defined to be 0.38. The Lagrange method and Penalty method (penalty parameter is 1.0) were run one after another. The motion of the target was governed by a node in the center of the sphere. In this simulation, a -6 unit displacement along the y direction was assigned to the target. The running results can be found in Fig.A6. It is evident that the results predicted by Lagrange and penalty methods are in great agreement with each other. More importantly, both of the two results fit pretty well with Hertzian model. The effectiveness of the two algorithms for contact simulation was validated accordingly.

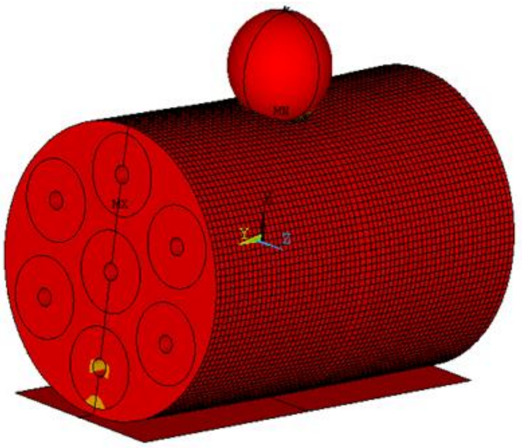

Figure A4. Schematic of nanoindentation.

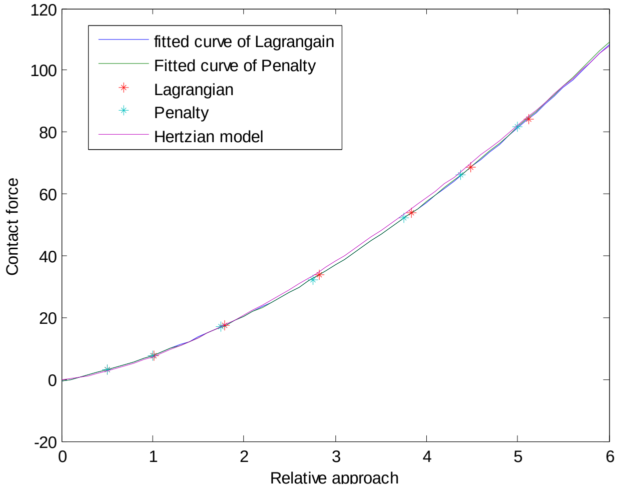

Figure A5. Comparison of simulation results.

A.3. Finite element formulation of adhesive forces into the contact system

A.3.1. Formulation of governing equation for adhesive contact

In order to include the adhesion into the FE model, the work done by the adhesive forces need to be incorporated into the governing equation Eq.A.13. The Lennard-Jones potential is employed to calculate the interatomic forces between two planes as follows,

$$\phi(r)=\varepsilon(\frac{r_0}{r})^{12}-2\varepsilon(\frac{r_0}{r})^{6} \tag{A.17}$$

where r is the distance between two atomic planes, r_0 is the equilibrium distance where force is 0, ε is the adhesion energy density.

The Lennard-Jones potential has been widely used as an approximation for van der Waals force. Then the work done by the adhesive forces can be calculated by

$$w_{adh} = \iiint\limits_{V} \delta\boldsymbol{u} \cdot \beta_k \boldsymbol{b_k} dV \tag{A.18}$$

where $\delta\boldsymbol{u}$ is the variation of displacement; β_k is molecular density in the volume domain; the subscript k can be c or t, which represent contactor and target, respectively; $\boldsymbol{b}_k$ is the body force vector raised from adhesion and it can be calculated by the following equations

$$\begin{gathered} \boldsymbol{b_c(x}_c\boldsymbol{)} = -\frac{\partial\phi_t}{\partial\boldsymbol{x_c}}, \phi_t(\boldsymbol{x_c}) = \int\limits_{V_t} \beta_t \phi(r) dV \\ \boldsymbol{b}_t\boldsymbol{(x}_t\boldsymbol{)} = -\frac{\partial\phi_c}{\partial\boldsymbol{x}_t}, \phi_c(\boldsymbol{x}_t) = \int\limits_{V_c} \beta_c \phi(r) dV \end{gathered} \tag{A.19}$$

The derivation of the two equations above can be found in the reference [92] By defining that $F = -\partial\phi / \partial r, \boldsymbol{r_1} = (\boldsymbol{x_1} - \boldsymbol{x_2}) / r, \boldsymbol{r}_2 = (\boldsymbol{x}_2 - \boldsymbol{x}_1) / r$, the body force vectors can be written into

$$b_1(x_1) = \int\limits_{V_2} \beta_2 F(r) \boldsymbol{r_1} dV_2, b_2(x_2) = \int\limits_{V_1} \beta_1 F(r) \boldsymbol{r}_2 dV_1 \tag{A.20}$$

Including the adhesion work in Eq. 20 in the governing equation for contact system (Eq. 15), we can obtain the governing equation for adhesive contact problem, which is

$$\sum_{k=c,t} [\int\limits_{V_k} grad(\delta\boldsymbol{u_k}) : \boldsymbol{\sigma}_k dv_k - \int\limits_{V_k} \delta\boldsymbol{u_k} . \beta_k \boldsymbol{b}_k dv_k - \delta \prod\nolimits_{ext,k}] = 0 \tag{A.21}$$

where $\delta \prod_{ext,k}$ means the work by external body and surface forces whose expression can be found in Eq. 15. It is noted that the governing equation is founded based on the current deformation state so the stress tensor in it is Cauchy stress and the molecular density is that in deformed volume. The governing equation can also be expressed by the quantities in original status as follows,

$$\sum_{k=c,t} [\int\limits_{V_{0k}} grad(\delta\boldsymbol{u_k}) : \boldsymbol{P}_k dV_{0k} - \int\limits_{V_{0k}} \delta\boldsymbol{u_k} . \beta_{0k} \boldsymbol{b}_k dV_{0k} - \delta \prod\nolimits_{ext,k}] = 0 \tag{A.22}$$

where $grad(\delta \boldsymbol{u_k})$ is gradient of displacement increment with respect to the original dimensions, $\boldsymbol{P_k}$ is the first Piola-Kirchhoff stress tensor, β_{0k} is the molecular density in the original volume.

In order to evaluate the work done by the adhesion, integration of six levels are needed which is very expensive in computation and challenging to perform in finite element implementation. With the purpose to simplify the integration of adhesion work, we introduce the method proposed in reference [92]. To interpret this method, we'll take the example to evaluate the body force at point $x_k$in the body V_k.(shown in Fig.A.7) Two procedures are included as follows

1). The point $x_k$is first projected towards the surface of the volume V_l. The projection line is perpendicular to the surface of the V_l. The projection point is labeled with x_p. The projection point $x_p$in the body $V_l$isnot a material point so it won't move with the material.

2). The body $V_l$is approximated with a flat half space on which the integration of adhesion work, as shown in Eq. A18, is performed.

The schematic of body force formulation can be found in Fig.A8. The determination of the projection point is actually the same as the algorithm stated in section A.2 to find the closest point. The projection direction is denoted by $-\boldsymbol{n_p}$,which is opposite to the normal direction of the projection point $x_p$on the surface of the body V_l. Then the body force acting on point $\boldsymbol{x_k}$can be obtained by the integration on the half space

$$\boldsymbol{b_k} = \pi \beta_l \varepsilon r_0^2 \left[\frac{1}{5} (\frac{r_0}{r_k})^{10} - (\frac{r_0}{r_k})^4 \right] \boldsymbol{n_p} \tag{A.23}$$

where$r_k$is the distance between x_k and x_p, which is the projection distance; β_l is the molecular densityat the projection point x_p.

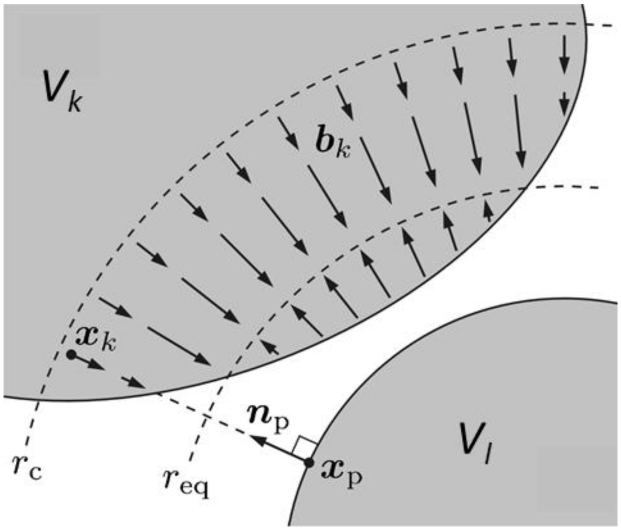

Figure A6. Schematic of body force formulation.

In order to find the expression which can be directly plugged into Eq.A.22, the governing equation built on the original volume, the Hamaker's constant was introduced: $A_H = 2\pi^2\beta_{01}\beta_{02}\varepsilon r_0^2$. Then Eq. A.23 can be rewritten into

$$\beta_{0k}\boldsymbol{b_k} = \frac{A_H}{2\pi r_0^4 J_l}\left[\frac{1}{5}(\frac{r_0}{r_k})^{10} - (\frac{r_0}{r_k})^4\right]\boldsymbol{n_p} \tag{A.24}$$

When the neighboring body V_l is unable to deform, then J_l in Eq.A.24 is 1. Now it is ready to plug the body force vector directly into the integration so that the adhesion work can be estimated. It can be concluded from the equation that the body force is mainly decided by two parameters, the adhesive force $A_H$and the adhesive range r_0. There is actually another way to evaluate the adhesion work, where the surface force is formulated instead of body force. This method sometimes works more efficiently than the body force method but the tendency to inaccuracy has been observed with this method when the adhesion increases. Constrained by the time, the surface force method won't be elaborated here. For more details of the surface force method, please read the reference [93].

A.3.2. Finite element implementation of adhesive contact

As the finite element model has been built above, the finite element implementation will be addressed in this section.

The domain over which the integration is to be performed was discretized into two different types of elements, the volume elements and the surface elements. For either of the two elements, the displacement vector and the displacement variation vector can be approximated by

$$\boldsymbol{u} = \boldsymbol{N_e}\boldsymbol{u_e}, \delta\boldsymbol{u} = \boldsymbol{N_e}\boldsymbol{v_e} \tag{A.25}$$

where the subscript e denote the quantities for an element, $\boldsymbol{u_e}$ and $\boldsymbol{v}_e$ are displacement and displacement variation vectors for an element, respectively; the matrix $\boldsymbol{N_e}$ can be calculated by the shape functions as below

$$\boldsymbol{N_e} = [N_1\boldsymbol{I}, N_2\boldsymbol{I}, ..., N_{ne}\boldsymbol{I}] \tag{A.26}$$

where $\boldsymbol{I}$ is a 3×3 identity matrix.

Invoking the displacement and displacement variation functions in Eq.A.25 into the weak form of governing equation, Eq. 23, the governing equation becomes a discretized matrix equation

$$\boldsymbol{v}^T[\boldsymbol{f_{int}} + \boldsymbol{f_{adh}} - \boldsymbol{f_{ext}}] = \boldsymbol{0} \tag{A.27}$$

where $\boldsymbol{v}$ is the virtual displacement of the nodes on elements, $\boldsymbol{f_{int}}$, $\boldsymbol{f_{adh}}$ and $\boldsymbol{f_{ext}}$ are the virtual work done by the internal strain, adhesive forces and external body and surface loads, respectively. They are all assembled from the vectors of individual elements.

According to Eq. A.27, we can obtain that

$$\boldsymbol{f_{int}} + \boldsymbol{f_{adh}} - \boldsymbol{f_{ext}} = \boldsymbol{0} \tag{A.28}$$

Generally speaking, the internal strain work and the adhesion work vary nonlinearly with the displacement vector. The internal force vector over a specific element can be expressed by

$$\boldsymbol{f}_{\text{int}}^{e} = \int_{\Omega_e} \boldsymbol{B}_e^T \boldsymbol{\sigma} dV \tag{A.29}$$

where $\boldsymbol{B_e}$ is the matrix that contains components of the derivative of the shape functions.

The virtual work done by the adhesive contact forces can be estimated by

$$\boldsymbol{f}_{adh}^{e} = -\int_{\Omega_e} \boldsymbol{N}_e^T \beta_k \boldsymbol{b}_k dV \tag{A.30}$$

A.3.3. Analysis of the finite element method for adhesive contact

In order to validate the effectiveness of the finite element model proposed above for adhesive contact in nanoscale, an example was taken where a sphere comes into contact with a flat surface. The bottom and the sides of the flat surface which is the block in Fig.A.9 are all fixed while the top surface of the block is free to motion and deformation. A predefined displacement was applied to the sphere and then a corresponding reaction force can be calculated by the finite element simulation. The simulation results by means of the finite element model introduced in this thesis was displayed in Fig.A7, where different surface energy density was used. As seen from it, the adhesive force came into play within a small region outside of the contact area. To further justify the accuracy of the finite element model, the simulation results were also plotted together with the results predicted by the analytical models of contact mechanics, which was demonstrated in Fig.A.8. The adhesive force is evidently observed from it. Most of all, the curve of simulation results fall between the JKR and DMT models. Thus the finite element model founded can work effectively. Particularly, the simulation can differentiate the approaching and separation processes, which can also be observed in nanoindentation experiments. However, the analytical results by JKR, DMT and Hertz models cannot tell the two processes from each other. The superiority of the finite element simulation is thus demonstrated.

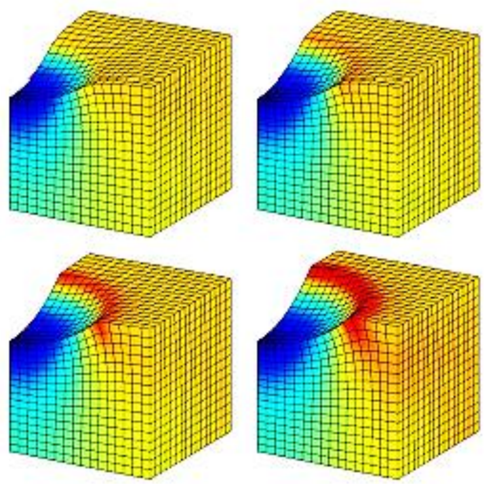

Figure A7. The simulation results of adhesive contact with different surface energy density.[93]

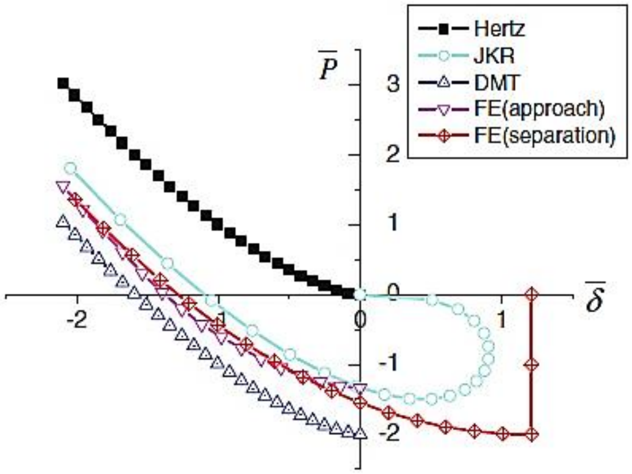

Figure A8. Comparison of FE simulation results and contact mechanics models.[93]